Clim Dyn
DOI 10.1007/s00382-011-1054-9

# Global off-line evaluation of the ISBA-TRIP flood model

**B. Decharme · R. Alkama · F. Papa · S. Faroux · H. Douville · C. Prigent**

Received: 26 October 2010 / Accepted: 21 March 2011


**Abstract** This study presents an off-line global evaluation of the ISBA-TRIP hydrological model including a two-way flood scheme. The flood dynamics is indeed described through the daily coupling between the ISBA land surface model and the TRIP river routing model including a prognostic flood reservoir. This reservoir fills when the river height exceeds the critical river bankfull height and vice versa. The flood interacts with the soil hydrology through infiltration and with the overlying atmosphere through precipitation interception and free water surface evaporation. The model is evaluated over a relatively long period (1986–2006) at 1° resolution using the Princeton University 3-hourly atmospheric forcing. Four simulations are performed in order to assess the model sensitivity to the river bankfull height. The evaluation is made against satellite-derived global inundation estimates as well as in situ river discharge observations at 122 gauging stations. First, the results show a reasonable simulation of the global distribution of simulated floodplains when compared to satellite-derived estimates. At basin scale, the comparison reveals some discrepancies, both in terms of climatology and interannual variability, but the results remain acceptable for a simple large-scale model. In addition, the simulated river discharges are improved in term of efficiency scores for more than 50% of the 122 stations and deteriorated for 4% only. Two mechanisms mainly explain this positive impact: an increase in evapotranspiration that limits the annual discharge overestimation found when flooding is not taking into account and a smoothed river peak flow when the floodplain storage is significant. Finally, the sensitivity experiments suggest that the river bankfull depth is potentially tunable according to the river discharge scores to control the accuracy of the simulated flooded areas and its related increase in land surface evaporation. Such a tuning could be relevant at least for climate studies in which the spatio-temporal variations in precipitation are generally poorly represented.

**Keywords** Land surface hydrology · Floodplains · River discharges · Evapotranspiration

B. Decharme (✉) · R. Alkama · S. Faroux · H. Douville
GAME–CNRM/CNRS - Météo-France, 42 av. G. Coriolis, 31057 Toulouse, France
e-mail: bertrand.decharme@meteo.fr

F. Papa
NOAA-CREST, City College of New York, New York, NY, USA

C. Prigent
CNRS/Laboratoire d'Etudes du Rayonnement et de la Matière en Astrophysique, Observatoire de Paris, Paris, France

*Present Address:*
F. Papa
Institut de Recherche pour le Developpement IRD-LEGOS, Toulouse, France

## 1 Introduction

The land surface hydrology represents an active component of the climate system (Dirmeyer 2000, 2001; Douville 2003, 2004; Koster et al. 2000, 2002) and is likely to influence the water and energy exchanges at the land surface, the ocean salinity and temperature at the mouth of the largest rivers (Durand et al. 2010), and the climate at least at the regional scale (Gedney et al. 2000; Douville et al. 2000a, b; Molod et al. 2004; Lawrence and Slater 2007; Alkama et al. 2008). These land surface processes are

Published online: 03 April 2011

parameterized in Continental Hydrologic Systems (CHSs). CHSs are composed by Land Surface Models (LSMs), which provide realistic lower boundary conditions of temperature and moisture in Atmospheric General Circulation Models (AGCMs), and now generally include River Routing Models (RRMs) which convert the runoff simulated by the LSMs into river discharge in order to transfer the continental fresh water into the oceans and then to close the global hydrological cycle.

At the global scale, many studies have focused on RRMs development (Vörösmarty et al. 1989; Liston et al. 1994; Miller et al. 1994; Hagemann and Dümenil 1998; Oki and Sud 1998; Arora and Boer 1999; Coe 1998; Ducharne et al. 2003). These models are generally based on simple budget equations representing the temporal variations of the water mass stored in each grid cell of a hydrological network determined according to the actual topography. This network is generally derived at coarse resolution (from 0.25° by 25° to 4° by 4°) except Coe's model (Coe 1998) that used a 5-min resolution. The main difference between these simple linear reservoir models is related to the processing of the river flow velocity that can be parameterized as:

- constant in space and time (Oki and Sud 1998) or using basin scale uniform transfer coefficients (Ducharne et al. 2003)
- constant in time but spatially distributed according to various relationships with the topography (Miller et al. 1994; Hagemann and Dümenil 1998; Coe 1998) or with both the mean annual river flow and the topography (Vörösmarty et al. 1989; Liston et al. 1994)
- variable in space and time according to the topography, the river geomorphology and the river water height using the Manning (1891) formula (Arora et al. 1999; Lucas-Picher et al. 2003; Ngo-Duc et al. 2007; Decharme et al. 2010)

Nevertheless, most of these models do not account for inland water bodies (Vörösmarty et al. 1989; Liston et al. 1994; Miller et al. 1994; Hagemann and Dümenil 1998; Oki and Sud 1998; Arora et al. 1999; Ducharne et al. 2003) or consider them as static (Coe 1998) while their evolution and variability have an important impact on the Earth's climate system.

Water bodies can be separated in two categories: anthropogenic and natural. Man-made inundated surfaces include reservoirs, rice fields and agricultural irrigation while natural inundated areas are related to river flooding, lakes, large ponds, and wetlands (bog, fen, mire, marshes). They have a strong influence on the annual cycle of river discharges in both tropical and high-latitude areas that emphasize their relevance for water resource management (Coe et al. 2002, 2008; Decharme et al. 2008). They affect the overlaying atmosphere through their relatively high evapo-transpiration that enhances latent versus sensible heat exchange with the atmosphere (Krinner 2003). Finally, through $CO_2$ and/or methane emissions, surface water bodies, especially wetlands, regulate the biogeochemical cycles that impact the climate evolution. Indeed, they are the world's largest source of methane and a major contributor to its inter-annual variability (Houweling et al. 1999; Matthews 2000; Bousquet et al. 2006; Ringeval et al. 2010) and could have contributed significantly to global warming since pre-industrial time (Shindell et al. 2004). Hence quantifying the distribution and variations of surface water bodies over the global land surface is a key question regarding climate change in terms of hydrological impacts as well as methane emissions (Bousquet et al. 2006). Consequently, recent efforts have been made to represent natural inland water surfaces in CHSs. Gedney et al. (2004) used an implicit representation in a LSM without any dedicated surface reservoir in order to estimate the potential feedback of wetland methane emissions on climate change. Other studies have proposed simple explicit parameterizations of flooded areas prescribing the residence time of water into pre-dimensioned reservoirs (Coe 1998; Coe et al. 2002; Krinner 2003; Güntner et al. 2007).

However, the recent development of new satellite observations and techniques (Alsdorf et al. 2007; Prigent et al. 2001, 2007; Papa et al. 2010a) shows that inland water bodies greatly vary in space and time and evolve with environmental and climate conditions. Some new modeling capabilities have been proposed to represent inland water bodies, or at least floodplains, at continental scale and at fine resolution. Coe et al. (2008) developed a distributed river model at 5-min resolution over the Amazon River in which the flood processes are parameterized using information from the 1 km resolution Shuttle Radar Topography Mission (SRTM) data set. Such fine resolution information provides physically based fractional flooding inundation of grid cells from a statistical representation of sub-grid-scale floodplain morphology. Over the same basin, Beighley et al. (2009) developed a modelling framework based on a flexible height resolution representation of land surface topography and a fluvial transport system that is capable of providing realistic channel and floodplains hydraulic characteristics on a daily time scale. Fan and Miguez-Macho (2010) proposed a simple hydrologic framework applied over North America at 30-s resolution to simulate the wetland and inland water bodies based on dynamic and prognostic groundwater water table depth that can support surface water bodies by maintaining a saturated substrate. Nevertheless, only the wetlands distribution and spatial extent was investigated in this study without the evaluation of their time-tendency or dynamic. At a coarse resolution (1° by 1°), Decharme et al. (2008)

developed a coupled LSM-RRM flood scheme over South-America to represent the floodplain dynamics and its impact on continental evapotranspiration and energy budget for large scale applications and climate modeling trough the use of a simple sub-grid topographic relationship between water volume and flooded area. At a similar resolution (0.5° by 0.5°), Dadson et al. (2010) proposed also a coupled LSM-RRM flood scheme over the Niger inland delta region based on sub-grid topographic statistics. In terms of model evaluation, the Coe et al. (2008), Decharme et al. (2008) and Dadson et al. (2010) schemes were the first to be evaluated using conjointly satellite-derived inundation estimates and in situ river discharge observations whereas in previous studies only the impact of the flood processes on river discharges was investigated (Coe 1998; Krinner 2003; Coe et al. 2002; Güntner et al. 2007; Beighley et al. 2009).

Focusing on Decharme et al. (2008), the simple river flood scheme attempts to represent the space–time variations of the large seasonal inundations at continental scale, but excluding lakes, large ponds and wetlands. The flood dynamics is described through the daily coupling between the Interaction Sol-Biosphère-Atmosphère (ISBA) LSM (Noilhan and Planton 1989) and the Total Runoff Integrating Pathways (TRIP) RRM (Oki and Sud 1998) including a prognostic flood reservoir added by Decharme et al. (2008). This reservoir fills when the river height exceeds the river bankfull height and vice versa. Its dimension evolves dynamically according to the flood water mass and the sub-grid topography in a given grid-cell. The reservoir interacts with the soil hydrology through infiltration and with the overlying atmosphere through precipitation interception and free water surface evaporation. The evaluation was made in off-line mode over South-America. Results showed that due to a basin-scale increase in surface evaporation, the monthly discharges over the Parana River basin were drastically improved while over the Amazon basin, the improvement on the simulated discharge was mainly related to the introduction of a delay in the timing of river flow through water store in the flooded area. In addition, an acceptable agreement between the simulated flooded areas and satellite-based inundation estimates was also found. These results were similar to that found at finer resolution by Coe et al. (2008) over the Amazon.

The main objective of the present study is to evaluate and to assess the robustness of this flood scheme at the global scale, an essential step before its use into coupled continent-atmosphere climate studies. This evaluation is done in off-line mode in which the ISBA-TRIP flood model is forced by the global meteorological data set provided by Princeton University (http://hydrology.princeton.edu) on a 3-hourly time step and at 1° resolution (Sheffield et al. 2006). As proposed by Coe et al. (2008) and Decharme et al. (2008) but only at regional to continental scale, the model outputs are evaluated against in situ river discharge measurements at 122 gauging stations as well as again satellite-derived inundation estimates from Prigent et al. (2007) now available from 1993 to 2004 (Papa et al. 2010a). This original evaluation strategy for a global scale study permits to evaluate both the floodplain climatology and variability, which is an important issue for possible feedbacks on the climate system, and for the impact of flood events on simulated river discharge and water budget. The ISBA-TRIP flood scheme is presented in Sect. 2. The experimental design, the specific parameters of the floodplain parameterization, and the different data sets are described in Sect. 3. Results are shown in Sect. 4 while a discussion and the main conclusions are provided in Sects. 5 and 6, respectively.

## 2 The ISBA-TRIP flood model

### 2.1 Review of ISBA-TRIP

ISBA is a relatively simple LSM that uses the force-restore method to calculate the time evolution of the surface energy and water budgets (Noilhan and Planton 1989). It includes a comprehensive sub-grid hydrology to account for the heterogeneity of precipitation, topography and vegetation in each grid cell. A TOPMODEL approach (Beven and Kirkby 1979) has been used to simulate a saturated fraction, $f_{sat}$, where precipitation is entirely converted into surface runoff (Decharme et al. 2006). Infiltration is computed via two sub-grid exponential distributions of rainfall intensity and soil maximum infiltration capacity. Finally, a tile approach is used to represent land cover and soil depth heterogeneities (Decharme and Douville 2006a).

The original TRIP RRM was developed by Oki and Sud (1998) at the University of Tokyo. It was first used at Météo-France to convert the simulated runoff into river discharge using a global river channel network at 1° resolution. In the new ISBA-TRIP CHS (Decharme et al. 2010), TRIP takes into account a simple groundwater reservoir which can be seen as a simple soil–water storage and a variable stream flow velocity as proposed by Arora et al. (1999). This variable velocity, $v$ (m.s$^{-1}$), is computed via the Manning's formula:

$$v = \frac{\kappa}{n} R^{2/3} s^{1/2} \quad (1)$$

where $s$ (m.m$^{-1}$) is the downstream river height loss per unit length approximated as the river bed slope, $R$ (m) the hydraulic radius, $\kappa$ (m$^{-3}$.s$^{-1}$) a constant equal to 1, and n

the dimensionless Manning friction factor which varies from the upstream part to the mouth of each basin (see Sect. 3). The hydraulic radius is related to the stream water depth, $h_s$ (m), calculated from the stream water mass, $S$ (kg), assuming a rectangular river cross-section (Arora et al. 1999):

$$R = \frac{Wh_s}{W + 2h_s} \quad \text{where } h_s = \frac{S}{LW\rho_w} \tag{2}$$

where $\rho_w$ (kg.m$^{-3}$) is the water density, $W$ (m) the bankfull river width, and $L$ (m) the river length that takes into account a meandering ratio of 1.4 as proposed by Oki and Sud (1998). TRIP is then based on two prognostic equations for the stream reservoir and the groundwater reservoir, $G$ (kg):

$$\left| \begin{array}{l} \frac{\partial S}{\partial t} = Q_{in}^{S} + \frac{G}{\tau} - \frac{v}{L} S \\ \frac{\partial G}{\partial t} = Q_{sb} - \frac{G}{\tau} \end{array} \right. \tag{3}$$

where $Q_{sb}$ (kg.s$^{-1}$) is the deep drainage from ISBA, $Q_{in}^{S}$ (kg.s$^{-1}$) the sum of the surface runoff from ISBA within the grid cell with the water inflow from the upstream neighboring grid cells, and $\tau$ (s) the uniform and constant time delay factor of the groundwater reservoir which is fixed to 30 days. This last reservoir does not represent the groundwater dynamics but only delays the groundwater flow contribution to the surface river reservoir within a particular grid cell: the deep drainage is fed into the surface reservoir with a time delay factor of $\tau$. More details can be found in Decharme et al. (2010).

### 2.2 The flood scheme

As proposed by Decharme et al. (2008), a simple coupling between ISBA and TRIP is proposed and the floodplains are explicitly represented into the surface water and energy budgets computed by ISBA. A floodplain reservoir, $F$ (kg), is added in TRIP that is now based on three prognostic equations:

$$\left| \begin{array}{l} \frac{\partial S}{\partial t} = Q_{in}^{S} + \frac{G}{\tau} - \frac{v}{L} S - Q_{in}^{F} + Q_{out}^{F} \\ \frac{\partial G}{\partial t} = Q_{sb} - \frac{G}{\tau} \\ \frac{\partial F}{\partial t} = Q_{in}^{F} - Q_{out}^{F} + \left(P_f - I_f - E_f\right) \end{array} \right. \tag{4}$$

where $Q_{in}^{F}$ and $Q_{out}^{F}$ (kg.s$^{-1}$) represent the flood inflow and outflow, respectively, and $P_f$, $I_f$ and $E_f$ (kg.s$^{-1}$) the precipitation interception by the floodplains, the re-infiltration and the direct free water surface evaporation estimated by ISBA, respectively. $I_f$ occurs if the flooded fraction, $f_{flood}$, calculated according to the subgrid topography ("Appendix") is superior to the soil saturated fraction, $f_{sat}$, and depends on the soil maximum infiltration capacity. In other words, the floodplains cannot infiltrate the fraction of the grid-cell for which the soil is saturated. To a first approximation, it allows to simply represent the fact that the actual floodplains evolve according to the presence of shallow aquifer and water table depth variations.

As shown in Fig. 1a, a simplified rectangular geometry is assumed to represent the cross section between the floodplain and the river reservoirs in each grid cell. River flooding arises when the water height of the stream reservoir is higher than the critical bankfull height, $h_c$, and the flood outflow and inflow from this reservoir (Eq. 4) are given by:

$$\left| \begin{array}{l} Q_{in}^{F} = \frac{v_{in}}{W + W_f} M_f \\ Q_{out}^{F} = \frac{v_{out}}{W + W_f} \min\left(M_f, F\right) \end{array} \right. \tag{5}$$

where $W_f$ (m) is the floodplain width ("Appendix"), and $M_f$ (kg) the potential inflow (positive $M_f$) or outflow (negative $M_f$) assuming an equilibrium state between the stream and the floodplain water depth:

$$M_f = \rho_w L_f W \left(h_s - h_c - h_f\right) \tag{6}$$

where $L_f$ (m) and $h_f$ (m) are the length along the river and the depth of the floodplains, $h_s$ (m) the water height of the stream reservoir, and $h_c$ (m) the critical bankfull river height. $W + W_f$ represents the distance covered by $M_f$ from the stream to the floodplains or conversely. $v_{in}$ and $v_{out}$ (m.s$^{-1}$) are the flood inflow and outflow velocities computed using the Manning's formula:

$$v_{in,out} = \frac{s_{in,out}^{1/2}}{n_f} R_{in,out}^{2/3} \tag{7}$$

where $n_f$ is the Manning roughness coefficient for the floodplains that varies according to the vegetation type (Sect. 3) while $s_{in,out}$ (m.m$^{-1}$) and $R_{in,out}$ (m) are the inflow (or outflow) slope and hydraulic radius, respectively at the interface between the floodplain and the river stream. More details can be found in "Appendix". Note that over Greenland, variable flow velocity and floodplains are not activated and a constant flow velocity of 0.5 m.s$^{-1}$ is used.

## 3 Experimental design

### 3.1 TRIP specific parameters

As discussed in Decharme et al. (2010), a special attention has been paid to the computation of the river bed slope at

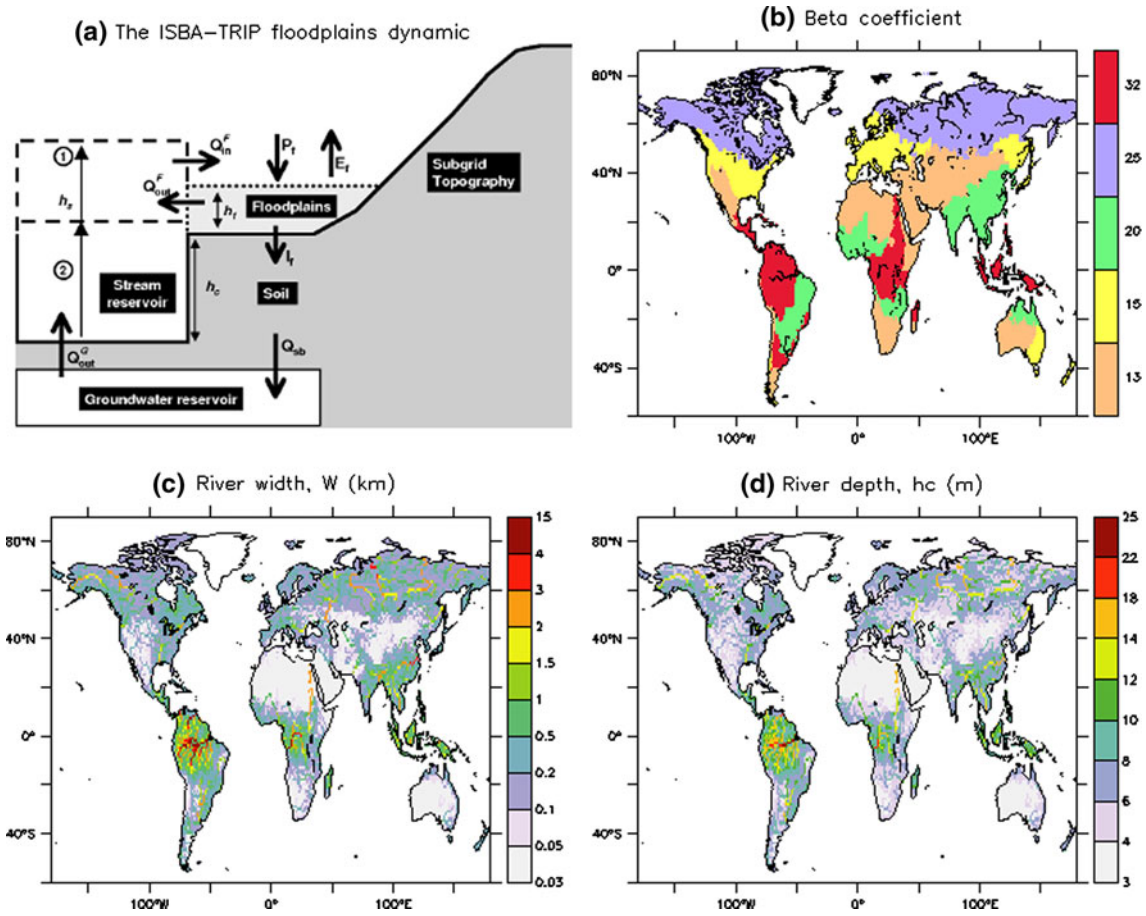


**Fig. 1** The ISBA-TRIP floodplain dynamics and the Global distribution of its specific parameters. **a** Schematic representation: (case 1) when the river depth, $h_s$, is above the critical river bankfull height, $h_c$, a flood inflow, $Q_{in}^{F}$, is computed; (case 2) when the flood decreases, $h_s$ becomes lower than the depth of the floodplains, $h_f$, and a flood outflow, $Q_{out}^{F}$, to the river is computed. See Sect. 2 for more details. **b** The $\beta$ coefficient used to compute the river width given in (**c**). **d** The bankfull river height. See Sect. 3 for more details

1° by 1° resolution. River bed slope is indeed a critical parameter to compute velocity via the Manning formula (Eq. 1). The STN-30p Digital Elevation Model (DEM) provided at 0.5° by 0.5° resolution by the ISLSCP2 database [http://islscp2.sesda.com] has been used. The STN-30p DEM was heavily edited to represent the actual elevation along the river network on a global scale, based on the aggregated HYDRO1 K DEM at 1 km resolution. Further adjustments were made to eliminate some of the unrealistic rapid slope changes in the STN-30p DEM along the global river network. As described in Decharme et al. (2010), the STN-30p DEM was finely interpolated at 1° by 1° resolution. To sum up, a 1° grid box is composed by four 0.5° grid boxes. If one of the four 0.5° grid boxes represents a mountain while the three other correspond to the valley where the major river flows, the interpolation to 1° resolution is only made via the averaging of the three valley's 0.5° grid boxes. This approach permits to compute elevation along the river at 1° resolution and to calculate the river bed slopes with a better accuracy.

In this study, the Manning friction factor varies arbitrary from 0.04 near the river mouth to 0.06 in the upstream grid cells. This factor can be defined as "the resistance of the bed of a channel to the flow of water in it". As discussed in Decharme et al. (2010), it is difficult to compute at global scale. It generally varies from low values for natural streams with deep pools as the river mouth to higher values for upstream small rivers. Common estimates give values around 0.024–0.075 for natural streams (Barnes 1967). Previous global studies generally used a global constant value of 0.035 (Arora et al. 1999; Arora and Boer 1999; Lucas-Picher et al. 2003), which has strong limitations given that the values greatly vary in natural streams. Here, it is assumed that upstream grid cells represented the narrower rivers and that the mouths could be seen as a "natural stream with deep pools" in each basin. As a

consequence, a linear relationship is taken between the Manning $n$ and the river stream order, $SO$, given by TRIP in each grid cell of a given basin:

$$n = n_{\min} + (n_{\max} - n_{\min})\left(\frac{SO_{\max} - SO}{SO_{\max} - SO_{\min}}\right) \quad (8)$$

where $n_{\max}$ and $n_{\min}$ are the maximum and the minimum value of the Manning friction factor (respectively equal to 0.06 and 0.04), $SO_{\min}$ and $SO_{\max}$ the minimum and maximum stream order in each basins of the TRIP network.

The river width is an important parameter because it is jointly used in the simulation of the river flow and the floodplain dynamics. It is computed over the whole TRIP network via an empirical mathematical formulation that generally describes a geomorphologic relationship between $W$ and the mean annual discharge at each river cross section (Knighton 1998; Arora et al. 1999; Moody and Troutman 2002):

$$W = \max\left(30, \beta \times Q_{yr}^{0.5}\right) \quad (9)$$

where $Q_{yr}$ ($m^3/s$) is the annual mean discharge in each grid cell estimated using the global runoff database from Cogley (2003). As shown in many studies, the $\beta$ coefficient can vary drastically from one basin to another (Knighton 1998; Arora et al. 1999; Moody and Troutman 2002). As for example, using width and discharge observations, Arora et al. (1999) found a value of 32 for the Amazon River while Moody and Troutman (2002) found 17 for the Mississippi River. In this study, $\beta$ is fixed for five different hydrological regions of the world as shown in Fig. 1b. $\beta$ is 32 for equatorial or sub-tropical basins, 25 for arctic or sub-arctic basins, 20 for "monsoon" basins, 15 for temperate basins, and 13 for semi-arid or arid basins. Each value has been chosen so that the resulting river mouths match the following values: 15,000 m for the Amazon (equatorial), 2,000–3,000 m for arctic rivers, 500–2,000 m for temperate rivers, 1,500–3,000 m for monsoon rivers, and less than 1,000 m for semi-arid or arid rivers. The spatial distribution of the river width is given in Fig. 1c while some calculated values are given in Table 1.

As shown in Decharme et al. (2008) over South-America, the key parameter for the floodplain parameterization is $h_c$, the critical river bankfull height. In this previous study, $h_c$ was computed via a linear relationship with the river width. Nevertheless, this previous formulation induces a drastic sharp transition in $h_c$ value at the basin boundary, especially in the upstream part of the Amazon. In this study, a non linear function is proposed:

**Table 1** Examples of river basin characteristics in the TRIP 1° by 1° network

| Basins | Area ($km^2$) | Lon | Lat | $\beta$ | Width (m) | $h_c$ (m) | $h_c$ − 25% | $h_c$ + 25% |
|---|---|---|---|---|---|---|---|---|
| Amazon | 6,134,937 | −50.5 | 0.5 | 32 | 14,755 | 25 | 18.75 | 31.25 |
| Congo | 3,751,344 | 12.5 | −5.5 | 32 | 6,860 | 19 | 14.25 | 23.75 |
| Mississippi | 3,245,654 | −90.5 | 29.5 | 15 | 2,112 | 13 | 9.75 | 16.25 |
| Parana | 3,007,044 | −58.5 | −34.5 | 20 | 2,872 | 14 | 10.5 | 17.5 |
| Nile | 2,961,360 | 30.5 | 30.5 | 32 | 2,511 | 14 | 10.5 | 17.5 |
| Ob | 2,958,911 | 70.5 | 66.5 | 25 | 2,936 | 14 | 10.5 | 17.5 |
| Yenisei | 2,603,497 | 83.5 | 71.5 | 25 | 3,658 | 15 | 11.25 | 18.75 |
| Lena | 2,335,590 | 124.5 | 73.5 | 25 | 2,934 | 14 | 10.5 | 17.5 |
| Niger | 2,119,052 | 6.5 | 5.5 | 20 | 1,531 | 12 | 9 | 15 |
| Amur | 1,864,936 | 140.5 | 53.5 | 15 | 1,700 | 12 | 9 | 15 |
| Yangtze | 1,827,110 | 120.5 | 31.5 | 20 | 3,679 | 15 | 11.25 | 18.75 |
| Mackenzie | 1,736,363 | −134.5 | 68.5 | 25 | 2,520 | 14 | 10.5 | 17.5 |
| Volga | 1,387,236 | 48.5 | 46.5 | 25 | 2,242 | 13 | 9.75 | 16.25 |
| Murray | 1,067,251 | −35.5 | 139.5 | 15 | 594 | 8 | 6 | 10 |
| Ganges | 1,029 593 | 88.5 | 22.5 | 20 | 2,521 | 14 | 10.5 | 17.5 |
| Orinoco | 958,945 | −61.5 | 9.5 | 32 | 5,621 | 18 | 13.5 | 22.5 |
| Yukon | 844,111 | −164.5 | 62.5 | 25 | 2,299 | 13 | 9.75 | 16.25 |
| Danube | 804,386 | 29.5 | 45.5 | 15 | 1,597 | 12 | 9 | 15 |
| Mekong | 801,386 | 106.5 | 10.5 | 20 | 2,706 | 14 | 10.5 | 17.5 |
| Sénégal | 429,686 | 16.5 | −15.5 | 20 | 575 | 8 | 6 | 10 |
| Loire | 118,046 | −1.5 | 47.5 | 15 | 541 | 8 | 6 | 10 |
| Rhône | 95,461 | 4.5 | 44.5 | 15 | 694 | 9 | 6.75 | 11.25 |

The basin name, the basin drainage area (*Area* in $km^2$), the locations (longitude, *Lon*, and latitude, *Lat*), the basin $\beta$ coefficient (Eq. 8), and the width (m) are given. The different values of the bankfull height at each river mouth are also shown

$$h_c = W^{1/3} \quad (10)$$

A global distribution of $h_c$ is given in Fig. 1d. However, as described in the next section, two additional sensitivity experiments are also done with $h_c \pm 25\%$ leading to an increase or a decrease in bankfull height from about 1 m to 6 m (Table 1).

Finally, the Manning roughness coefficient for the floodplains, $n_f$, is computed by using the spatial distribution of the 12 vegetation types at 1° resolution specified according to the 1-km ECOCLIMAP data base of Météo-France (Masson et al. 2003). Indeed, the vegetation has generally a non-negligible impact on this roughness coefficient (Thomas and Nisbet 2006) and a simple solution is used:

$$n_f = \sum_{i=1}^{12} (vegt_i \times n_i) \quad (11)$$

where $n_i$ is the floodplain roughness coefficient corresponding to one vegetation type (Table 2), and $vegt_i$ the grid-cell fraction of each vegetation types. As shown in Fig. 2, $n_f$, is larger in densely vegetated areas and lower for sparser vegetated regions.

### 3.2 Experiments

The experimental design is similar to Decharme et al. (2008). An off-line hydrological simulation with the flood scheme (*FLD*) is compared to a control experiment without floodplains (*CTL*). In addition, two sensitivity experiments to the $h_c$ parameter are also performed globally using $h_c \pm 25\%$. These two simulations permit to present a sensitivity study to the $h_c$ parameter. In Decharme et al. (2008), a comparable sensitivity experiment to $h_c$ over South-America basins had suggested that the model is relatively robust, without any particular tuning, but such conclusion must be investigated and confirmed at global scale. ISBA and TRIP are integrated at 1° resolution using 30-min and 1 h time step, respectively over 1983–2006 where the first 3 years are considered as spin-up. Every day, the total runoff (surface runoff + deep drainage) simulated by ISBA is fed into TRIP which returns to ISBA the grid-cell floodplain fraction and the flooded water mass in order to calculate $P_f$, $I_f$, $E_f$ (Eq. 4) and the surface energy budget.

**Table 2** The 12 vegetation types specified according to the 1-km ECOCLIMAP data base and the corresponding floodplain roughness coefficient, $n_i$, used in Eq. 11

| | Vegetation types | Floodplain roughness coefficient |
|---|---|---|
| 1 | Bare soil | 0.035 |
| 2 | Rocks | 0.035 |
| 3 | Permanent snow and ice | 0.035 |
| 4 | Forest and trees | 0.075 |
| 5 | Coniferous forest | 0.100 |
| 6 | Broadleaf evergreen forest | 0.100 |
| 7 | C3 crops | 0.050 |
| 8 | C4 crops | 0.050 |
| 9 | Irrigated crops | 0.050 |
| 10 | Grassland | 0.050 |
| 11 | Tropical grassland | 0.075 |
| 12 | Peat bogs and Irrigated grass | 0.075 |

The global meteorological forcing is provided by Princeton University (http://hydrology.princeton.edu) at a 3-hourly time step and 1° resolution. This data set is based on the National Center of Environmental Prediction-National Center for Atmospheric Research (NCEP-NCAR) reanalysis. Sheffield et al. (2006) carried out corrections of the systematic biases in the 6-hourly NCEP-NCAR reanalyses via hybridization with global monthly gridded observations. In addition, the precipitation was disaggregated in both space and time at 1° resolution via statistical downscaling and at 3-hourly time step using information from the 3-hourly Tropical Rainfall Measuring Mission (TRMM) data set. More details about this forcing product can be found in Sheffield et al. (2006). The 3-hourly precipitation from Sheffield et al. (2006) is hybridized to match the monthly value from the Global Precipitation Climatology Center (GPCC) Full Data Product V4 (http://www.dwd.de). As shown by Decharme and Douville (2006b), the GPCC climatology appears to be a better product to perform global hydrological applications.

The land surface parameters used by ISBA are specified according to the 1-km resolution ECOCLIMAP database developed at CNRM (Masson et al. 2003). The soil textural properties are given by the Harmonized World Soil Database of the Food and Agricultural Organization at 1 km resolution (FAO 2009). Vegetation parameters are defined using two vegetation data sets: the Corine Land Cover Archive at 250 m resolution over Europe and from the University of Maryland (Hansen et al. 2000) data set elsewhere at 1 km. All topographic information is specified according to the 30-arcsecond resolution GTOPO30 data set (http://eros.usgs.gov/products/elevation/gtopo30/gtopo30.html) and the 1 km resolution HYDRO1 K product (Verdin and Greenlee 1996; http://eros.usgs.gov/#/Find_Data/Product_and_Data_Available/gtopo30/hydro).

### 3.3 Evaluation data sets

Over the evaluation period (1986–2006), the simulated discharges are compared to gauging measurements from the HyBAm data set (http://www.mpl.ird.fr/hybam/) for the

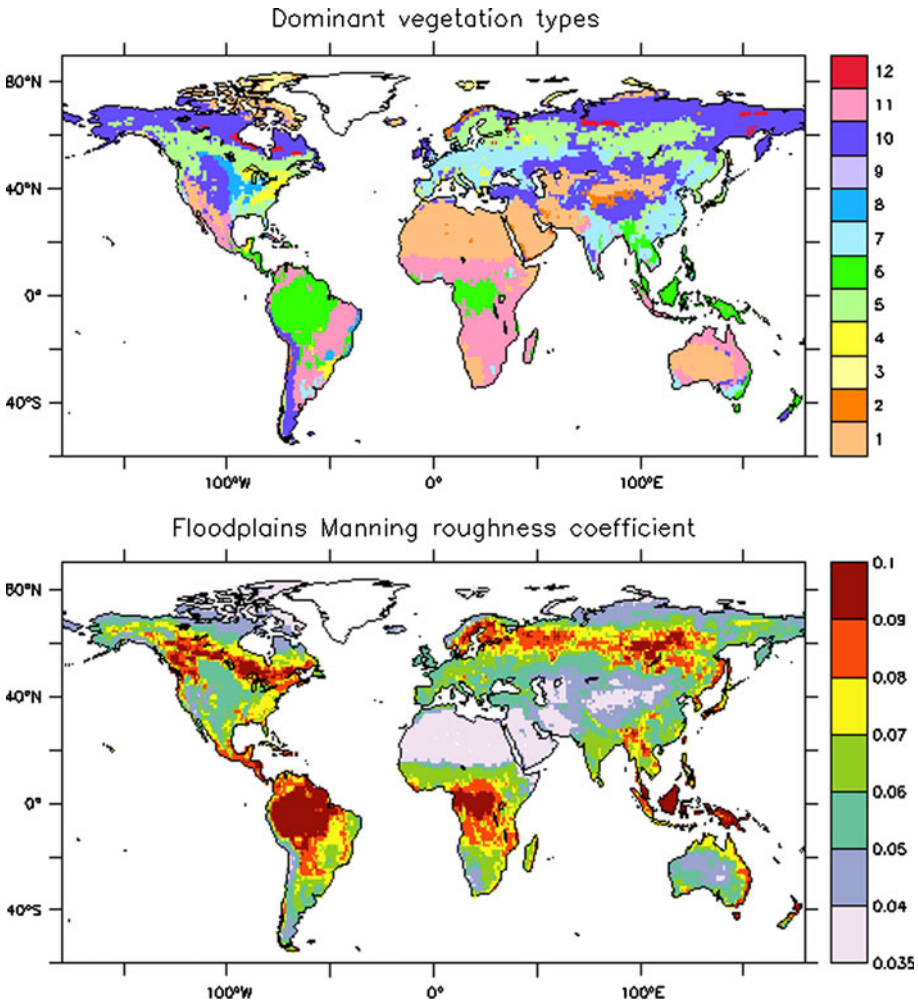


**Fig. 2** Spatial distribution of the dominant vegetation types at 1° resolution specified according to the 1-km ECOCLIMAP data (*top*) and the associated floodplain Manning roughness coefficient (*bottom*). The 12 vegetation types are described in Table 2

Amazon, the R-ArticNet database (University of New Hampshire; http://www.r-arcticnet.sr.unh.edu/v3.0/index.html) for high latitude basins, the Bangladesh Water Development Board data set for the Ganges as described in Papa et al. (2010b), and elsewhere from the Global Runoff Data Center (GRDC; http://www.grdc.sr.unh.edu/index.html). This evaluation data set combines in total 122 gauging measurements distributed over the globe (Fig. 3). Only sub-basins with drainage areas of at least $10^5$ km$^2$ and with a minimum observed period of 4 years are kept.

In addition, the satellite-derived inundation estimates are used to evaluate the spatial distribution and the time evolution of the simulated flooded areas over the 1993–2004 period (Prigent et al. 2007; Papa et al. 2010a). This data set quantifies at the global scale the monthly variations of the distribution of surface water extent at ~25 km sampling intervals. As described in detail by Prigent et al. (2001, 2007), it is derived from a complementary suite of satellite observations: Normalized Difference Vegetation Index (NDVI) given by the Advanced Very High Resolution Radiometer (AVHRR); active microwave from the European Remote Sensing (ERS-1) scatterometer backscatter at 5.25 GHz; and finally, passive microwave emissivities between estimated from the

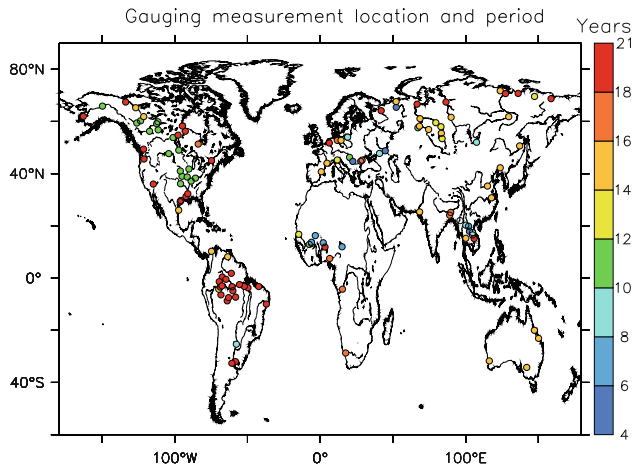


**Fig. 3** Location of the 122 gauging stations used for the evaluation. The *color* on each station represents the number of year of monthly data available, beginning in January 1986

Special Sensor Microwave/Imager (SSM/I) by removing the contributions of the atmosphere (water vapor, clouds, rain) and the modulation by the surface temperature, using ancillary data from visible and infra-red satellite observations from the International Satellite Cloud Climatology Project (ISCCP) and the National Centers for Environmental Prediction (NCEP) reanalysis. Global monthly-mean surface water extent data set is created with a 0.25° spatial resolution at the equator and is currently available from 1993 to 2004 (Prigent et al. 2007; Papa et al. 2010a). In the present study, this data set is then interpolated at 1° resolution and named hereafter *P07*. The global distribution of the *P07* mean inundated areas from 1993 to 2004 is given in Fig. 4a.

Because P07 does not make distinction between the diverse anthropogenic and/or natural water bodies while the ISBA-TRIP output must be compared with floodplain areas only, two additional data sets are used to hybridize *P07* in order to conserve information on flood interannual variability only: the Global Lakes and Wetland Database (GLWD) and the Monthly Irrigated and Rainfed Crop Areas around the year 2000 (MIRCA2000) database. The GLWD data (Lehner and Döll 2004) gives the global distribution of 12 types of surface water bodies as lakes, wetland and floodplains at 30arc second resolution (∼1 km at the equator). In this study, this product is interpolated at 1° resolution for lake, reservoir, and bog,

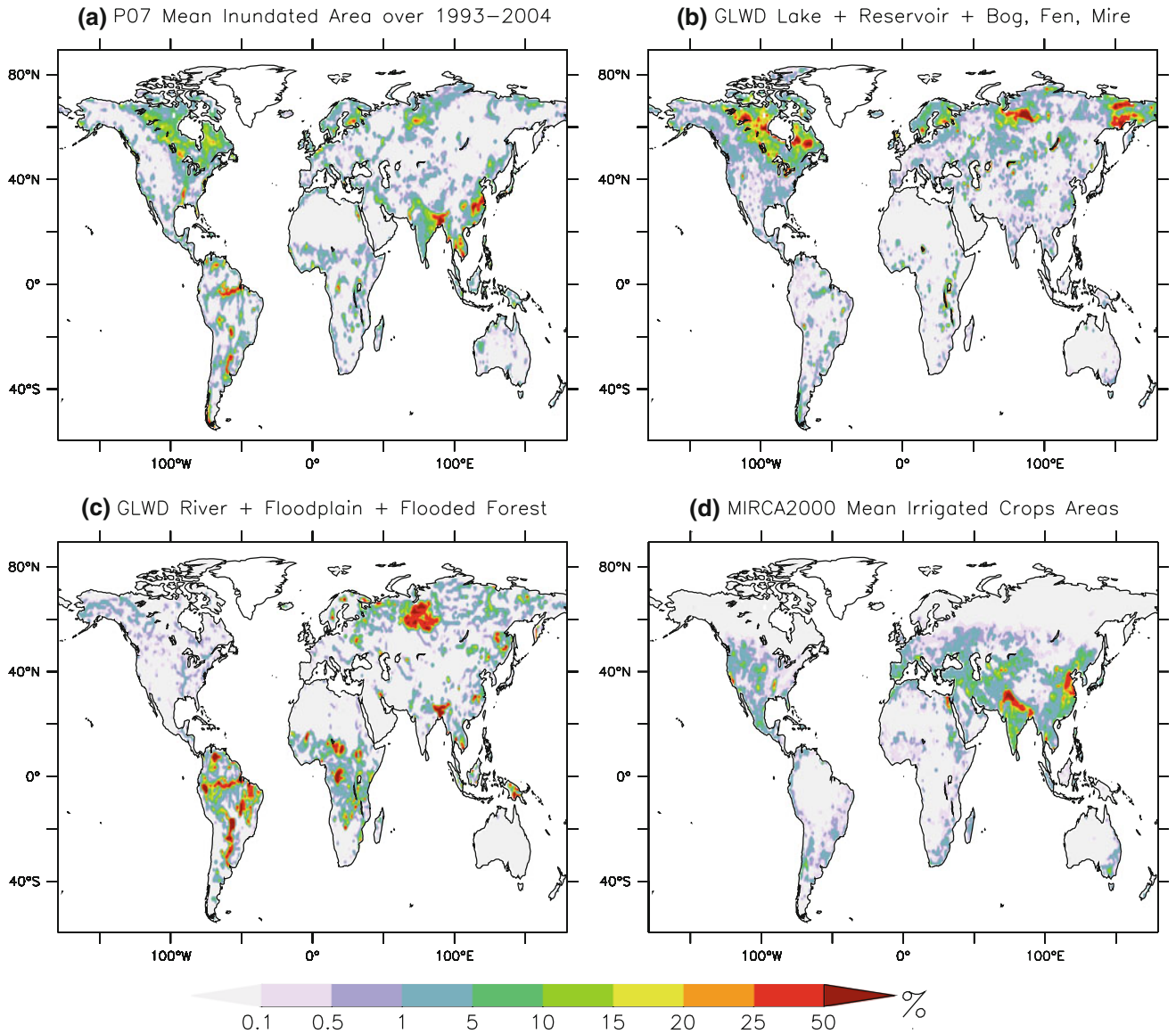


**Fig. 4** The different data sets used for the floodplain evaluation. **a** The global distribution of the P07 1993–2004 mean inundated extent. **b** The lakes, reservoirs, bogs, fens and mires from the GLWD database. **c** The GLWD rivers, floodplains and flooded forest areas. **d** The MIRCA2000 mean irrigated crop extent

fen and mire types as shown in Fig. 4b as well as for river, floodplain and flooded forest types as shown in Fig. 4c. The MIRCA2000 product (Portmann et al. 2010) provides both irrigated and rainfed crop areas of 26 crop classes for each month of a year around the year 2000 at 5arc minute resolution (~9.2 km at the equator). This product, which represents the sum of the 26 irrigated crop classes, is also interpolated at a 1° resolution and the global distribution of the annual maximum is given in Fig. 4d.

Figure 4 shows that *P07* cannot be directly compared with the simulated floodplain extents because it makes no distinction between floodplains and other surface water bodies. *P07* is then hybridized with the GLWD and the MIRCA2000 products to build an alternative product more comparable with the model simulations. This hybridization is carried out following two steps. First, the GLWD lakes, and bogs, fens and mires areas, $L_{GLWD}$, as well as the MIRCA2000 annual cycle $I_{mth}$, are subtracted from *P07* where the GLWD rivers, floodplains and intermittent lake/floodplain areas, $F_{GLWD}$, exist:

$$P_{07/GM}(t) = \delta \times \max[0, P07(t) - L_{GLWD} - I_{mth}] \quad \begin{cases} \delta = 1 & \forall F_{GLWD} > 0 \\ \delta = 0 & \forall F_{GLWD} = 0 \end{cases} \tag{12}$$

where $t$ (month) is the time and $P_{07/GM}$ the new final product.

## 4 Results

### 4.1 Flooded area

Figure 5 shows the comparison between the mean annual cycles of both the $P_{07/GM}$ inundated areas and the simulated

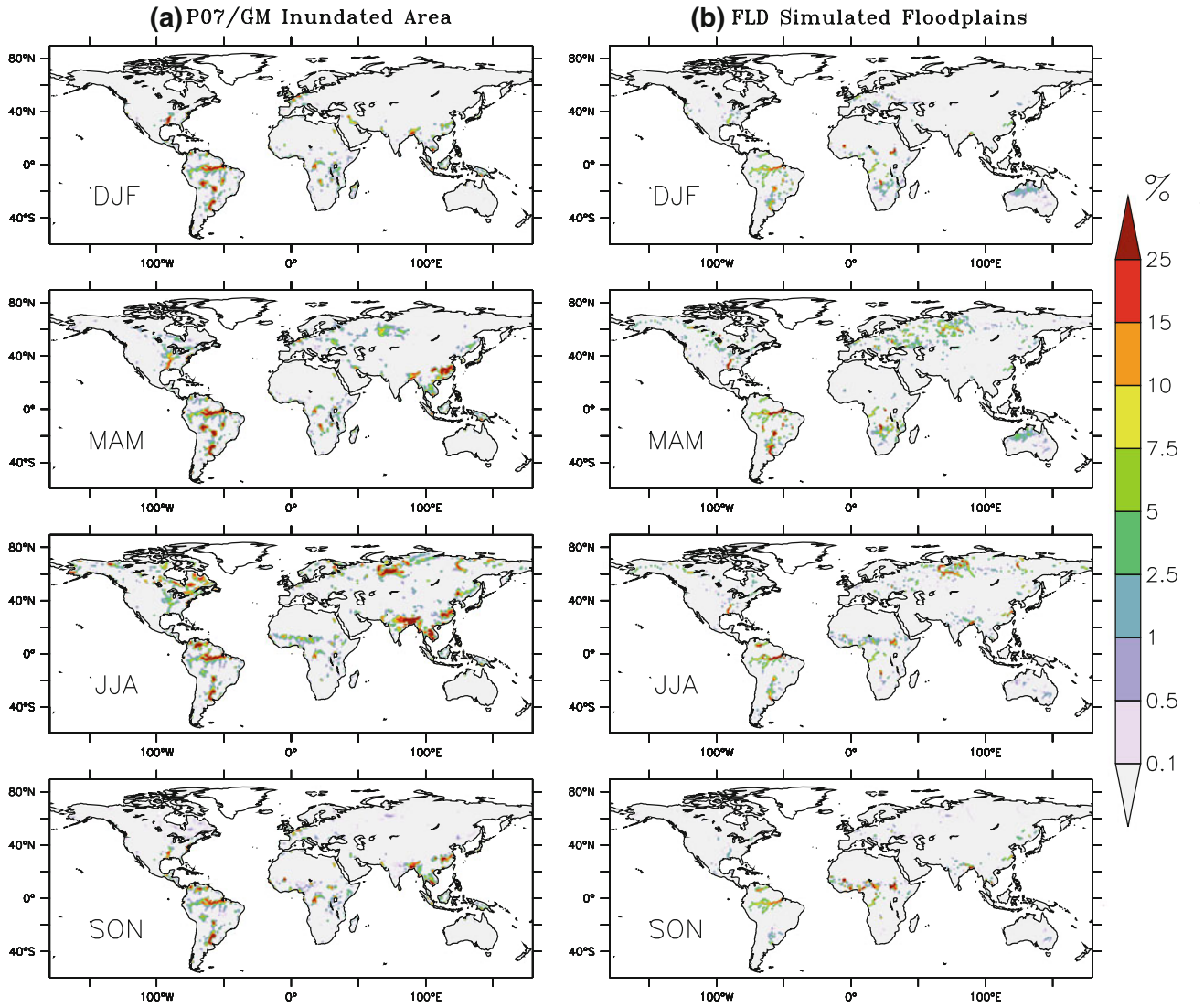


**Fig. 5** Spatial distribution of the mean annual cycles of both the $P_{07/GM}$ inundated areas (**a**) and the simulated FLD floodplains (**b**)

*FLD* floodplains. For each season, the global distribution of the floodplains simulated by *FLD* appears robust even if the simulated flooded areas seem to be underestimated especially over South Asia and Northern Canada. The comparison of *FLD* with the two sensitivity experiments ($h_c \pm 25\%$), based on the 1993–2004 mean flooded areas and given in Fig. 6, underlines the impact of the river bankfull height on the simulated flooded areas. As expected, a lower $h_c$ induces larger floodplains and inversely. Following Eq. 6, if $h_c$ decreases (increases), the potential inflow into the floodplain reservoir increases (decreases) according to Eq. 6, and then the resulting flooded areas also increase (decrease). Note that $h_c + 25\%$ drastically underestimates $P_{07/GM}$ globally while $h_c - 25\%$ is in better agreement except over Europe and Russia where the flooded areas appear too dense.

Figure 7 shows the basin-averaged annual cycles of monthly floodplain fractions. Over the Arctic basins (Mackenzie, Ob, Lena), the main difference between *P07* and $P_{07/GM}$ is linked to the important density of lakes, especially over the Mackenzie basin, and bogs, fens and mires elsewhere (Fig. 4b). The flooded areas are smaller over East Siberia (Lena) than over the Ob and/or Mackenzie basins, and generally located near the river stream (Fig. 6a). At these high latitudes, according to Fig. 5, the *FLD* simulated flooded area seems to be underestimated, especially during summer (June–July–August). In addition, the simulated flooded area starts earlier than the satellite-derived estimates. Over Central and/or Eastern Europe basins, the main difference between *P07* and $P_{07/GM}$ is linked to the presence of lakes and reservoirs over the Volga basin and irrigation over the Danube. Over the Volga basin, the *FLD* simulated flooded areas are overestimated during spring but the mean annual cycle is in agreement with satellite-based estimates. The same behaviour is observed over the Danube with larger

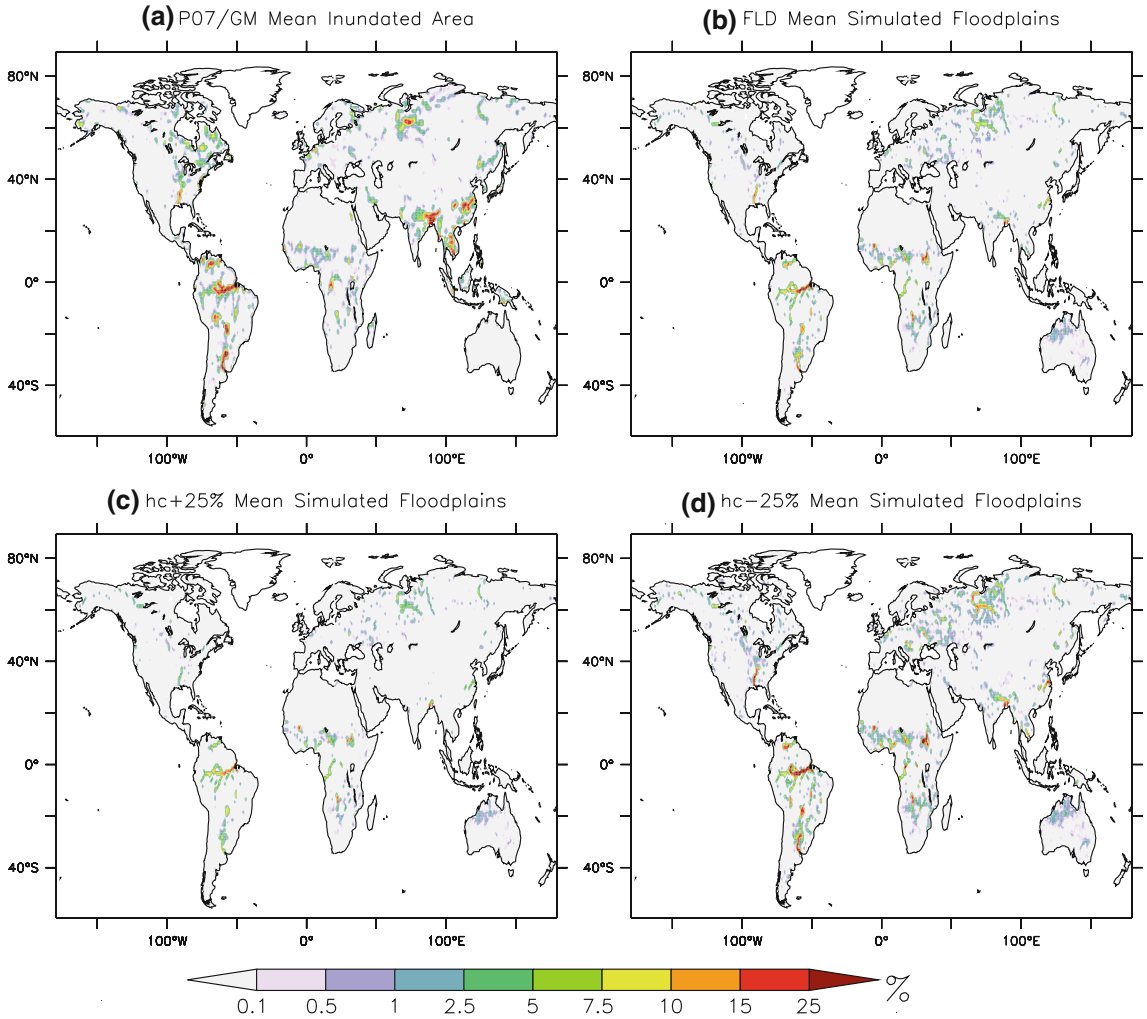


**Fig. 6** Spatial distribution of the annual mean inundated areas estimated by $P_{07/GM}$ (**a**), simulated by FLD (**b**), and computed with $h_c \pm 25\%$ (**c** and **d**)

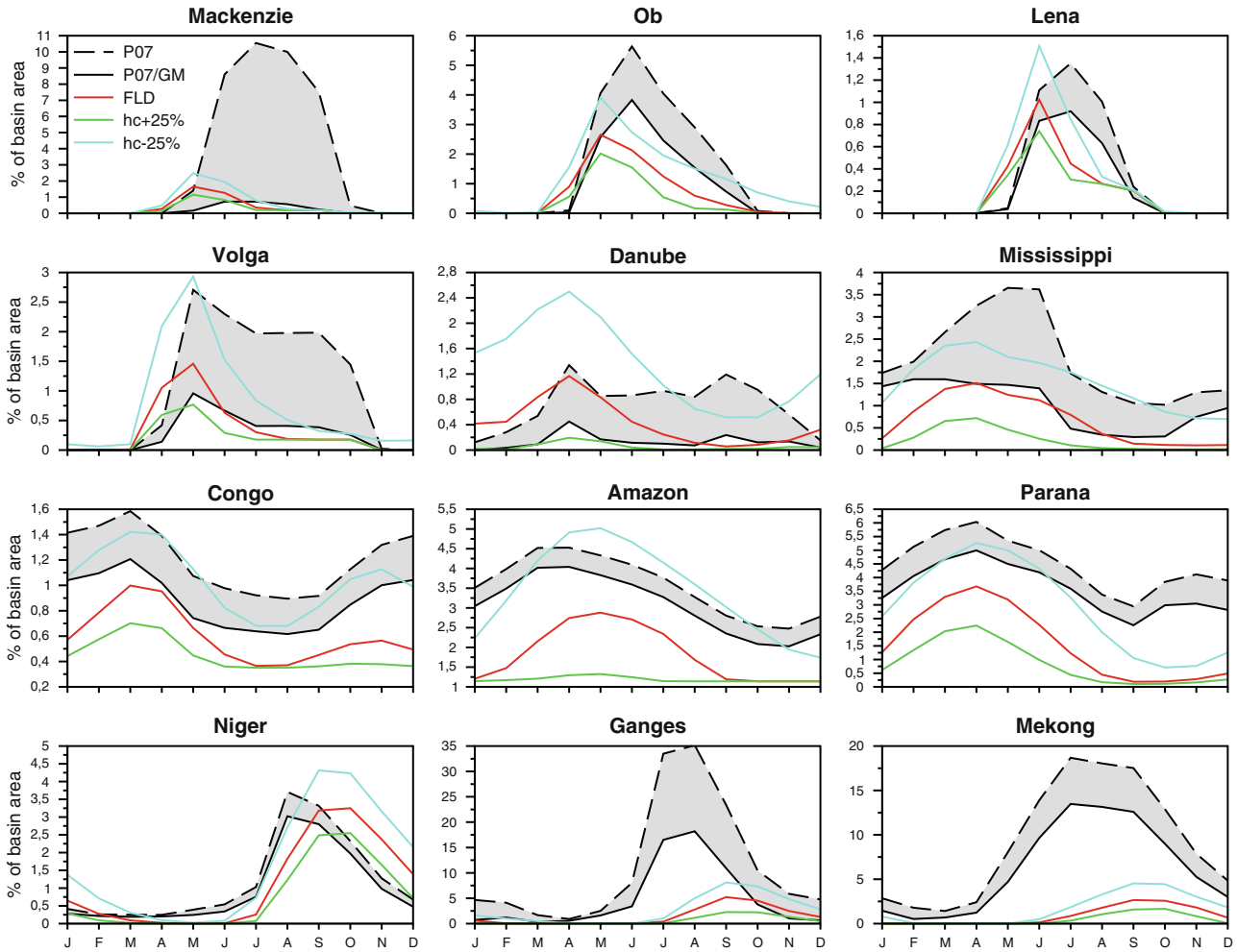


**Fig. 7** Comparison over major river basins between the basin-averaged annual cycles of simulated and estimated flooded areas over the 1993–2004 period. *P07* is in *dashed black line*, $P_{07/GM}$ in *black*, FLD in *red*, and $h_c \pm 25\%$ in *green* and *cyan*. Note that the maximum value on the *Y*-axis is highly variable from one basin to the other

differences but still in the $P07/P_{07/GM}$ estimated range. Over North America (Mississippi), the main $P07/P_{07/GM}$ difference is due to irrigation and the Mississippi simulated flooded fractions are relatively consistent with $P_{07/GM}$. Over Africa (Congo, Niger), a small fraction of lakes explains the $P07/P_{07/GM}$ difference. The Congo basin exhibits small floodplain areas and *FLD* is slightly underestimated. Over the Niger, while the amplitude of the simulated annual cycle appears acceptable, the *FLD* flooded areas start later and shows a too long persistence of the flooding season. Over South America (Amazon, Parana), the small $P07/P_{07/GM}$ difference is linked to the presence of lakes. The *FLD* simulated floodplains are generally underestimated. Over South Asia (Ganges, Mekong), the $P07/P_{07/GM}$ difference is mainly due to intensive irrigation. The *FLD* simulated floodplains are poorly reproduced with a clear underestimation and a flooded season that starts too late ($\sim$2–3 months later). Some explanations will be given in the discussion section. Regarding the sensitivity of $h_c$, the difference between *FLD* and $h_c \pm 25\%$ appears non-negligible everywhere. According to Fig. 6 and despite the general poor results over South Asia, $h_c + 25\%$ accentuates the *FLD* underestimation while $h_c - 25\%$ attempts to generally overestimate the simulated flooded areas except over the Mackenzie, the Mississippi, the Congo and the Parana where the simulated annual cycles seem to be better reproduced.

Moving to inter-annual variability, Fig. 8 shows the basin-averaged anomalies of the floodplain extent for $P_{07/GM}$, *FLD* and $h_c \pm 25\%$. The correlation and Root Mean Square Error (RMSE) for each experiment are also given. Generally speaking, the monthly anomalies are reasonably reproduced by *FLD*, especially over the Ob, Mississippi, Congo, Niger, Parana and Mekong basins even if these results cannot be considered satisfactory due to some poor correlation scores. The simulated flooded areas

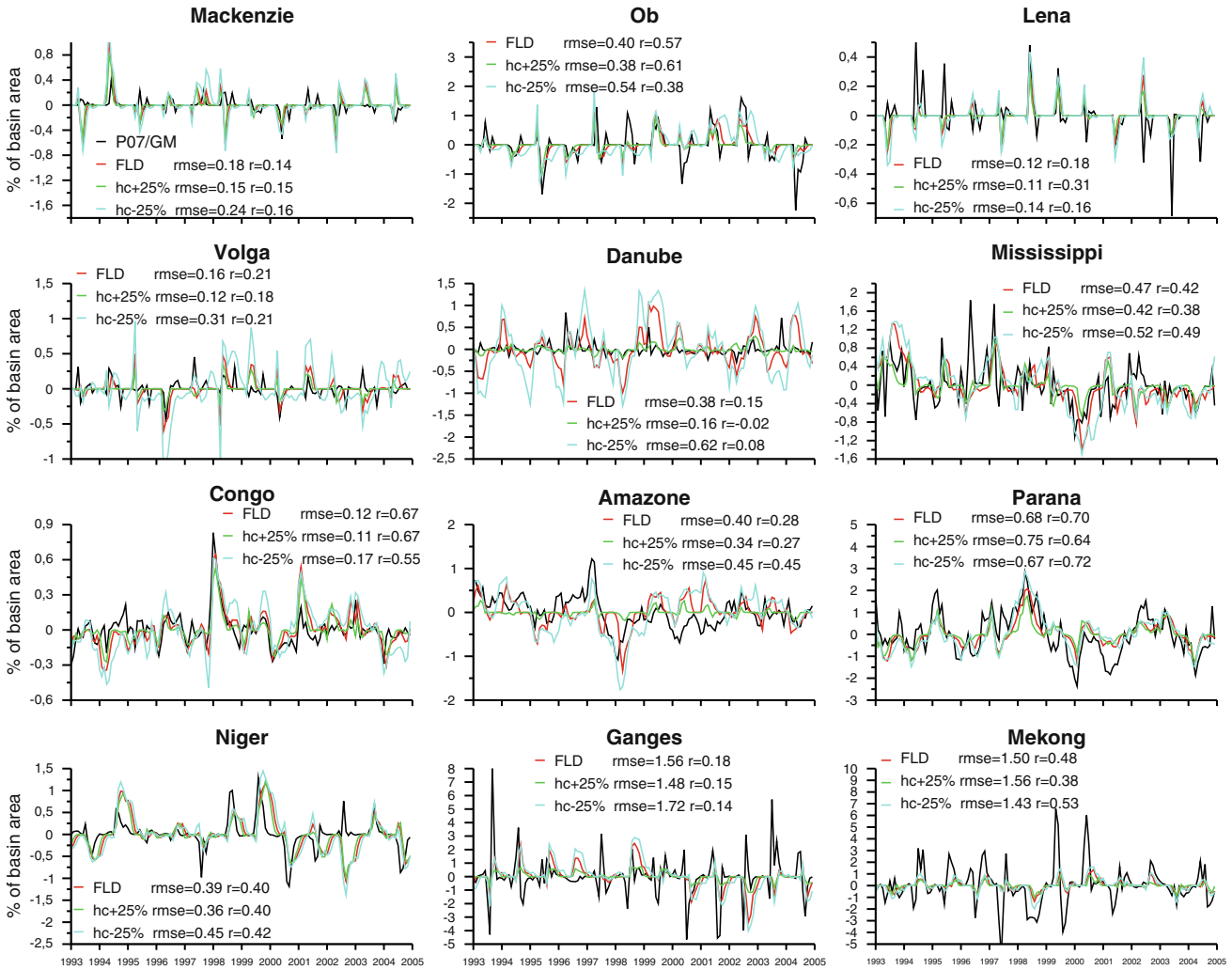


**Fig. 8** Comparison between the major basin-averaged simulated and estimated (*black line*) floodplain anomalies over the 1993–2004 period. The Root Mean Square Error (RMSE) and the correlation ($r$) are given for each simulation. Notations are the same than in Fig. 7

are smoothed when $h_c$ increases ($h_c + 25\%$) and then the RMSE scores are generally improved to the detriment of the monthly correlations. The main exception is observed over Siberia (Ob, Lena) where all scores are improved. Conversely, a decrease in $h_c$ ($h_c - 25\%$) increases the signal variability and then favors the correlations to the detriment of RMSE scores. Nevertheless, over all basins the sensitivity of $h_c$ remains generally relatively weak compared to the model error.

## 4.2 River discharges

It is now well known that seasonal flooding affects the river flow in many regions of the world from tropical to high latitude basins. Without the parameterization of flooding and their variations, CHSs tend to drastically overestimate Tropical and/or West African river discharges, which can be mainly related to the non representation of direct evaporation from free surface water bodies (Ngo-Duc et al. 2005; Decharme and Douville 2007; Decharme et al. 2008; Alkama et al. 2010). Over Arctic basins and especially the Ob and Mackenzie Rivers, large floods occur in May/June when the mass of water in the river increases due to snow melting. Consequently, a significant part of the water is not available for flowing and flooding limits the stream flow velocity compared to basins with more negligible floodplain processes (Yenisey, Lena). For example, over the Ob, large floods appear after the snowmelt period and can cover an important part of the basin, especially at the confluence of the Ob and the Irtysh (Figs. 5 and 7). The observed flow velocity is generally limited to 0.5 $m.s^{-1}$ due to the significant amount of water stored in these large floodplains (Kouraev et al. 2004; Frappart et al. 2010) whereas without flooding, this velocity can be drastically faster and can reach 1 $m.s^{-1}$–2 $m.s^{-1}$ (Arora et al. 1999; Decharme et al. 2010). Such processes that delay and attenuate the peak

discharge during large floodplain storage are also dominant over the Amazon basin (Coe et al. 2008; Decharme et al. 2008).

In this section, the simulated river discharges with (*FLD*) and without (*CTL*) flooding are now compared to gauging measurements. The present evaluation stage is important for hydrological applications as well as for future climate studies. Beside the direct evaluation of the simulated discharge scores, it permits to assess the interaction between the floodplains and the river flow as well as to evaluate indirectly the ISBA-TRIP water budget. This evaluation is done with the help of the most popular skill scores used in hydrology. These scores are: the annual discharge ratio criterion ($Ratio = \overline{Q_{sim}}/\overline{Q_{obs}}$), the RMSE, and the efficiency (*Eff*) (Nash and Sutcliffe 1970) criterion that measures the model ability to capture the monthly discharge dynamics. This last skill score is defined as follows:

$$Eff = 1.0 - \frac{\sum \left(Q_{sim}(t) - Q_{obs}(t)\right)^2}{\sum \left(Q_{obs}(t) - \overline{Q_{obs}}\right)^2} \quad (13)$$

where $\overline{Q_{obs}}$ represents the observed temporal mean. *Eff* can be negative if the simulated discharge is very poor and is above 0.5 for a reasonable simulation.

Figure 9 shows the global distribution of the difference between the *CTL* and *FLD* discharges in terms of annual ratio, efficiency, and monthly anomaly RMSE. The annual ratio is reduced (*FLD-CTL ratio* difference inferior to −0.05 in Fig. 9b) over 35% of the 122 gauging stations and mainly where this annual ratio is superior to 1.3 (25% of all stations). As it will be shown later, this decrease in annual discharge is related to the increase in continental evapotranspiration via the direct evaporation of the floodplains. The efficiency scores are increased (*Eff* difference superior to 0.05 in Fig. 9d) over 50% of all stations and only reduced (*Eff* difference inferior to −0.05) for 5 stations. The monthly anomaly RMSE scores are also improved (RMSE difference inferior to −0.01 in Fig. 9f) over 50% of all stations and only deteriorated (RMSE difference superior to 0.01) for 4 stations. In other words, *FLD* reduces the annual ratio especially over the stations where the *CTL* discharge overestimations are the largest (Fig. 9a). This fact is particularly relevant over Africa, Australia, and South America. As discussed before, over these regions this decrease in simulating river discharges is mainly responsible to the general positive impact on both the efficiency scores (Fig. 9d) and the monthly anomalies RMSE (Fig. 9f). Elsewhere, when an improvement is found, it is mainly due to a weaker peak in the river flow related to the floodplain storage. Conversely, some score deteriorations appear over Eastern Siberia (Lena, Amur) and near the mouth of the Mississippi River where the flooded areas are the largest (Fig. 6a, b). As shown in Fig. 9a, the Lena (or Amur) River discharges are clearly underestimated by *CTL*. So, even if *FLD* induces a slight decrease in river discharges, this decrease is sufficient to impact the efficiency scores. Over the Mississippi, the simulated floodplains seem to be too important at least near the downstream part of the basin.

As shown in Fig. 10 which represents the global distribution of the $h_c$ sensitivity on the simulated river discharges in terms of efficiency and monthly anomalies RMSE, an increase in $h_c$ and then a decrease in simulated flooded areas (Fig. 5c) improve these skill scores (+0.15 for *Eff* and −0.02 for RMSE) near the mouth of the Mississippi basin (Fig. 10a,c). Conversely, a decrease in $h_c$ and then an increase in simulated flooded areas (Fig. 5d) attempt to improve the scores over many regions of the globe. Exceptions are found over Siberia, the Amazon, South Europe, a part of South Asia and accordingly the downstream part of the Mississippi basin. The efficiency scores are increased ($h_c$ − 25%-*FLD Eff* difference superior to 0.05 in Fig. 10b) over 45% of all stations and only reduced (*Eff* difference inferior to −0.05) over 15%. The monthly anomaly RMSE scores are also improved (RMSE difference inferior to −0.01 in Fig. 10d) over 30% of all stations and only deteriorated (RMSE difference superior to 0.01) over 10%. These results underline the non-negligible impact of the $h_c$ value on the quality of the simulated discharges.

Focusing on the downstream station of the major world river basins, Fig. 11 compares the mean annual cycle of the simulated and observed discharges. The skill scores given on each plot are calculated over the actual signal and the entire period, and not over the annual cycle. The comparison between *FLD* and *CTL* confirms the general improvement of the simulated discharges pointed out by Fig. 9 with the use of the flood scheme. Over the Volga, the Danube, the Parana, the Niger and, to a lesser extent, the Congo River basin, this improvement is mainly related to a decrease in annual discharge ratio. This process is also relevant over the Mackenzie, the Ob or the Amazon basins but the improvement is mainly due to a better simulation of the river flow peak as already discussed. Exceptions are found over the Lena and the Mississippi, and to a lesser extent over the Ganges and the Mekong basins. Over the Lena, as already said, the simulated streamflow is clearly underestimated and a slight decrease in river discharges (due to simulated floodplains) is sufficient to impact the skill scores independently of the value of $h_c$. However, over the Lena, the Ganges and the Mekong basins the *FLD* simulation remains acceptable with regards to the *CTL* model errors. For example over the Ganges basin, while the annual peak of discharge is more consistent in *FLD* than in *CTL*, *FLD* conserves the general weakness found in *CTL*

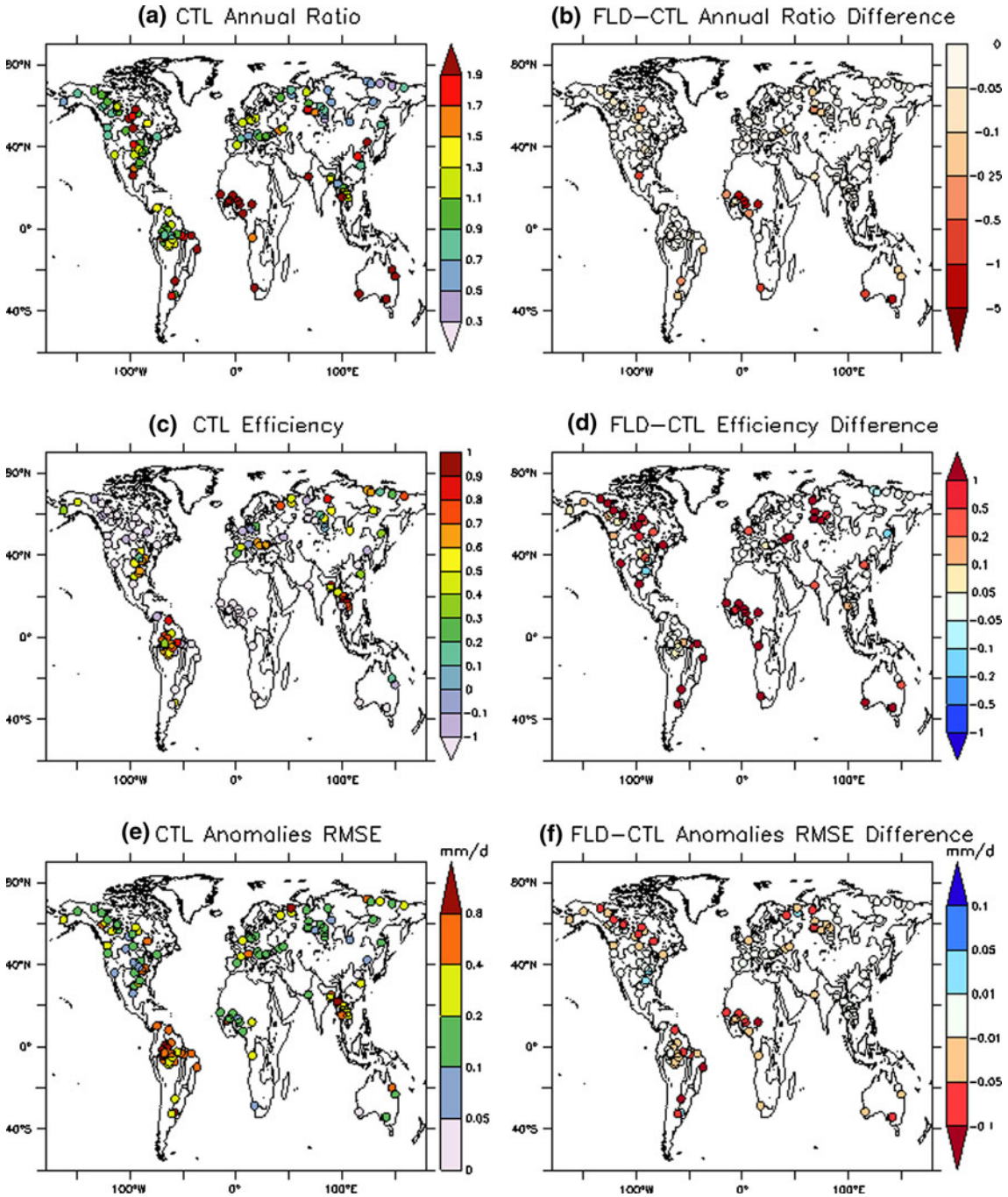


**Fig. 9** Comparison between the simulated monthly discharge with (FLD) and without (CTL) the flood scheme at each 122 gauging station. The CTL annual ratio (**a**) and efficiency (**c**) in terms of absolute values as well as the RMSE in terms of monthly anomalies (**e**) are given. The difference with the FLD scores is also shown (**b**, **d**, **f**)

where the high discharge season starts later and remains longer than in the observed discharges. This result is in agreement with the same drawback found in simulated floodplain extent (Fig. 7). The good scores given by the $h_c + 25\%$ simulation compared to the others over the Mississippi basin confirm that the simulated flooded areas are too large near its downstream part. Finally, Fig. 11 confirms that a decrease in $h_c$ and then an increase in simulated flooded areas can improve the quality of the simulated discharges over many rivers of the globe. Over non-improved basins (Siberian rivers, Danube, Mississippi, Amazon and Ganges), the decrease in $h_c$ induces too large floodplains and then smoother and unrealistic simulated annual cycle.

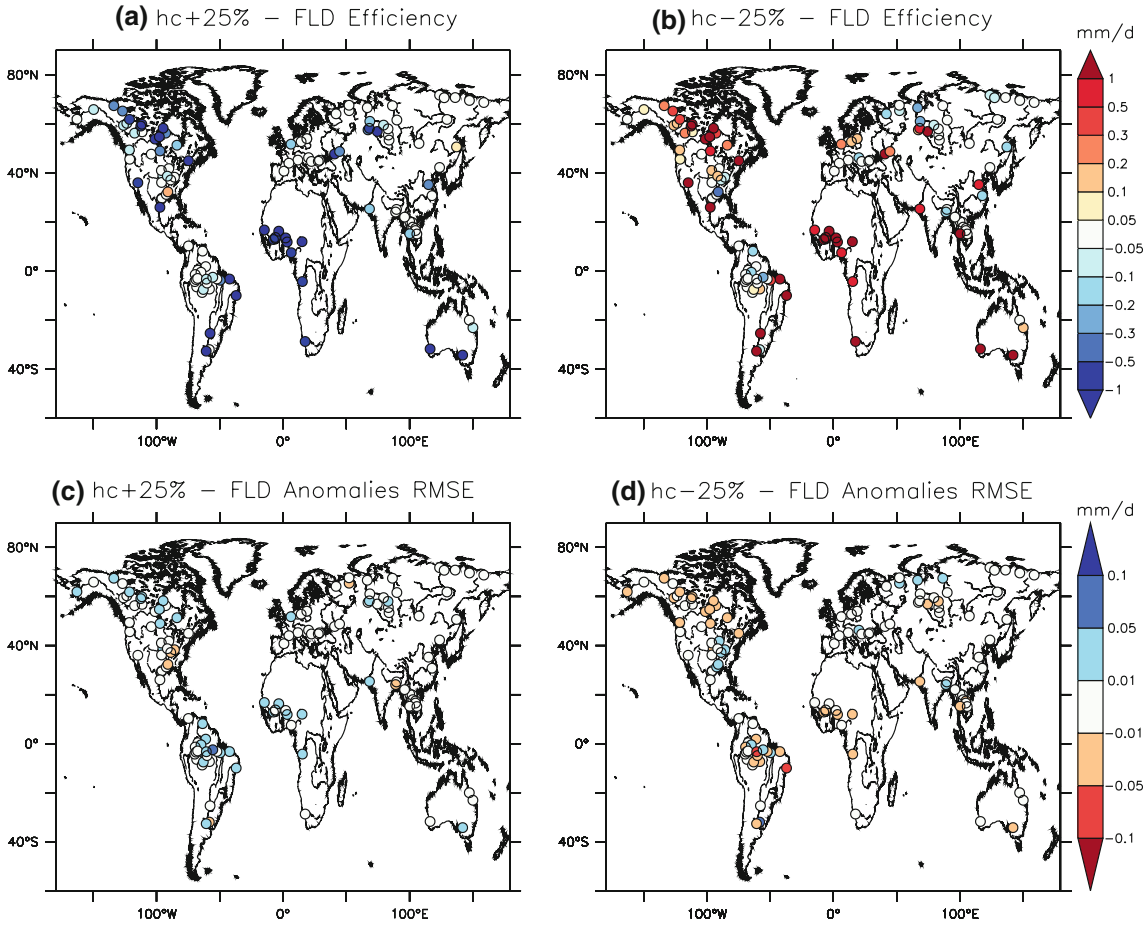


**Fig. 10** Sensitivity of the simulated monthly discharge to the river bankfull height at each 122 gauging station. The difference between simulations with $h_c \pm 25\%$ and FLD is given in terms of efficiency (**a**, **b**), and monthly anomalies RMSE (**c**, **d**)

Moving to the discharge inter-annual variability, Fig. 12 shows the comparison between the simulated and observed discharges over the same gauging stations than in Fig. 11. The RMSE and correlation of each simulation are also given. In general, *FLD* improves these scores and then the simulated inter-annual variability, which confirms results given in Fig. 9f. The main impacts are found over the Arctic basins (Ob, Mackenzie), South America (Amazon, Parana) and West Africa (Niger) even if the correlation is reduced. No significant change is observed over the Danube and South Asian basins, and except over the Mississippi basin, a slight improvement is found elsewhere. Regarding the sensitivity of $h_c$, beside some exceptions (Ob, Mississippi, Parana, Ganges) where one of the three floodplain simulations is clearly better than the others, the monthly discharges anomalies are generally not impacted by the value of $h_c$.

### 4.3 Water budget

The implementation of the flood scheme leads to a clear reduction in the simulated river discharges (from 5 to 20% compared to *CTL*) over some large river basins (Ob, Mackenzie, Volga, Mississippi, Parana, Niger, and Ganges), while others remain relatively unchanged (less than 5% compared to *CTL*). This reduction in river discharges is logically balanced by an increase in evapo-transpiration. Figure 13 compares the mean annual cycle of the *FLD* simulated evapo-transpiration with *CTL*. The global surface evaporation increase is around 2% and is especially important during spring (March, April, and May). Despite the fact that this increase can appear negligible in some cases, it can also be very important over some regions (North Canada, East Europe, West Siberia, South America or South Africa) as shown in Fig. 13. Regarding the sensitivity of $h_c$, the global surface evaporation increase is around 1% for $h_c + 25\%$ and 4% for $h_c - 25\%$, and it is also more important during spring. The fact that a decrease in $h_c$ induces a strong increase in evaporation is linked to the overestimation of the simulated flooded areas over West Siberia and Europe with $h_c - 25\%$ (Fig. 6d). With regards to these global values, the sensitivity of $h_c$ is also non-negligible on the land surface water budget.

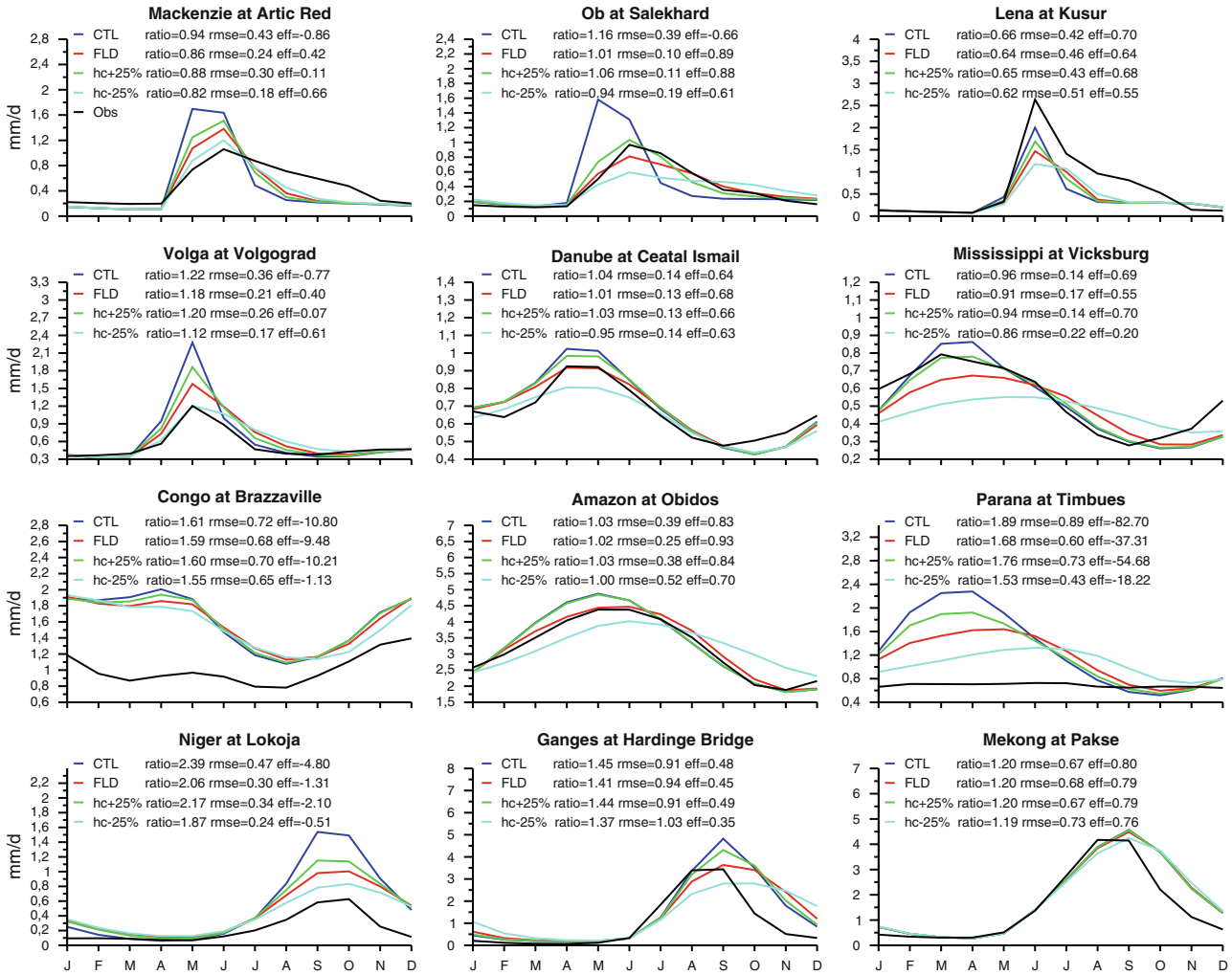


**Fig. 11** Comparison between the mean annual cycles of simulated and observed (*black line*) discharges over the same basins than in Fig. 7. Observations are in *black line*, CTL in *blue*, FLD in *red*, and $h_c \pm 25\%$ in *green* and *cyan*. The ratio, RMSE, and efficiency (*eff*) criteria given on each panel are calculated over the entire period and not over the annual cycle

## 5 Discussion

The results suggest that the proposed simple flood scheme generally provides a reasonable estimation of the spatio-temporal variability of the flooded areas. In addition, it improves the simulated river discharge over 50% of the 122 gauging stations while it deteriorates the skill score over only 4% of the cases. Elsewhere, the flood scheme has logically no impact because flood processes do not take place over all basins of the world. However, it must be recognized that the basin-scale comparison with satellite-derived flooded area estimates is not very impressive. As pointed out in the introduction, this study is the first attempt to evaluate a simple global two-way flood scheme developed at a coarse resolution where the flood process affects both the surface hydrology (floodplains and river flow) and the continental water and energy budgets. Such global work represents another step toward the physical representation of all inland water bodies in climate models. It is interesting to note that the results of Coe et al. (2008) over the Amazon basin, calculated with a finer resolution model, are coherent with this study and confirm the difficulties to accurately simulate together the floodplains and the discharge dynamics.

Some deficiencies appear throughout this evaluation. The simulated floodplains are generally underestimated and over some basins (Africa, South-Asia, Pantanal) the discharges remain drastically overestimated. It can be partially due to uncertainties in the precipitation forcing with regards to the small density of GPCC rain gauges in these regions (Decharme and Douville 2006b). Other causes can be related to some important processes not represented in ISBA-TRIP. The man-made irrigation (especially over South Asia) and/or dams can alter the river flow and increase the continental evapo-transpiration (Sacks et al. 2009). Deep and large aquifers relatively uncoupled to the

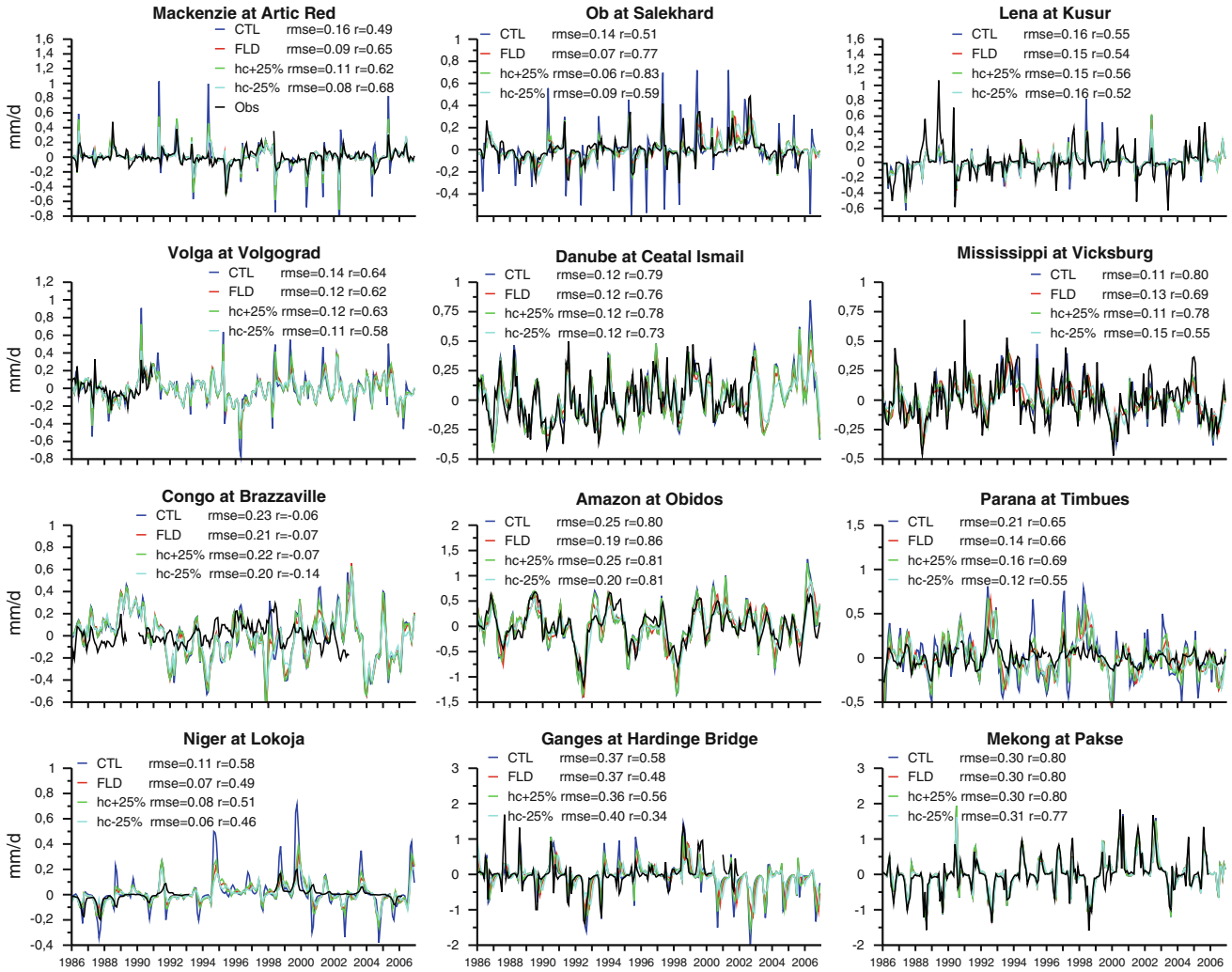


**Fig. 12** Same as in Fig. 10 but for the interannual variability. The RMSE and the correlation ($r$) are given for each experiment

river over arid or semi-arid basins, such as the Niger, contribute to limit the drainage inflow to the river (Leduc et al. 1997, 2001). Conversely, shallow aquifers support and feed surface water bodies when the water table depth reaches the surface (Fan and Miguez-Macho 2010). In ISBA, the water table depth evolution is simply parameterized thought a TOPMODEL approach. In TRIP, the deep reservoir does not represent the groundwater dynamics but only delays the groundwater flow contribution to the surface river reservoir within a particular grid cell. As a consequence, dynamical aquifer processes are not represented in this study. This fact may partly explain the general underestimation of the simulated floodplains.

Over the West Siberian basins, the well known precipitation bias in the GPCC data (Decharme and Douville 2006b) induces a general underestimation of both simulated flooded areas and discharges that does not permit to evaluate the scheme correctly. However, such underestimation could be also attributable to the presence of deep permafrost not represented in ISBA in which only the superficial soil ice (from 20 to 35 cm depth) related to the maximum penetration depth of the thermal diurnal wave (Boone et al. 2000) is parameterized. The permafrost prevents deep drainage and favors the formation of surface water bodies (wetlands, lakes…). This accumulation of surface water can also contribute to feed the floodplains (Kouraev et al. 2004; Price et al. 2005). In addition, all simulations over the Arctic basins show that the simulated flood starts earlier than the satellite-derived ones (Fig. 7). Over these regions, the floodplains and river discharges are fed mainly by the springtime snowmelt (Papa et al. 2007, 2008). Considering that the simulated and observed discharges are in phase (Fig. 11), the fact that the floodplains appear earlier in ISBA-TRIP is likely not due to an earliness of the snowmelt timing simulated by ISBA. As shown by Alkama et al. (2010) with the same configuration of the ISBA-TRIP model and the same atmospheric forcing than in the present study, the simulated snowmelt timing was

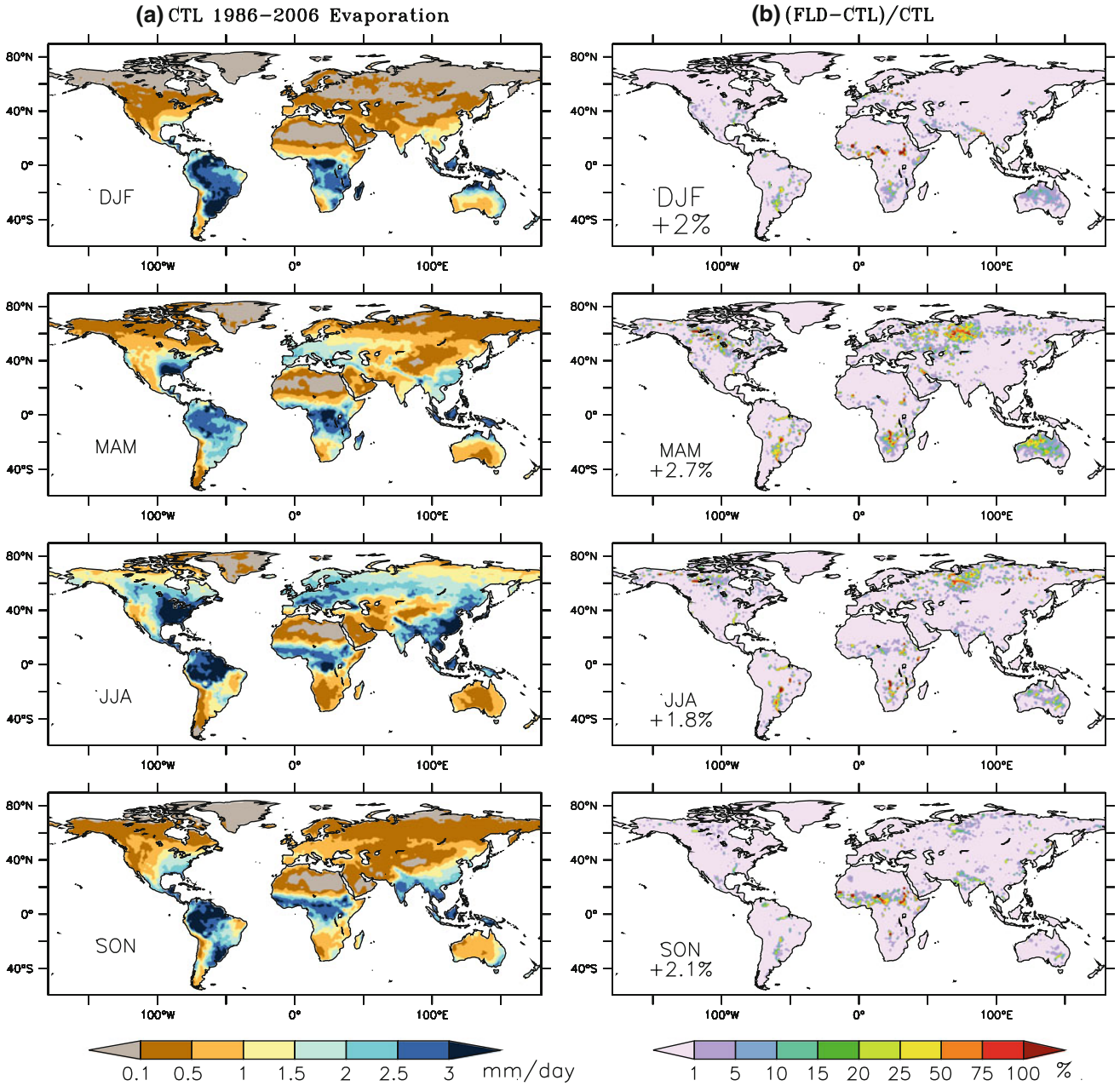


**Fig. 13** Impact of the flood scheme on the evapotranspiration mean annual cycle computed by ISBA over the 1986–2006 period. **a** Global distribution of the CTL evapotranspiration. **b** Comparison in % between CTL and FLD

well reproduced when compared to the National Snow and Ice Data Center (NSIDC; http://nsidc.org/) data. However, in these regions, P07 results might be questionable. Because the microwave measurements are sensitive to the snow cover, a snow and ice mask based on the same NSIDC data is applied over the Northern Hemisphere to avoid confusion between snow cover and snow-free pixels (Papa et al. 2007, 2008). An overestimated snow mask might impact the satellite-derived estimates and could be the cause of this slight difference.

The main model deficiencies appear over South Asia (Ganges, Mekong) where the simulated floodplains are drastically underestimated even compared to $P_{07/GM}$ in which the significant irrigated areas have been removed to *P07*. This rice irrigation is intensive after the monsoon season, from the end of September to December (Sacks et al. 2009; Portmann et al. 2010). Consequently, the fact that $P_{07/GM}$ shows important inundated areas throughout the year is relatively surprising, especially over the Indochina peninsula (Mekong) and at the confluence of the

Ganges–Brahmaputra rivers: in these regions, the multi-satellite method might encounter some difficulties in accurately discriminating between very saturated moist soil and standing open water and might overestimate the actual fraction of inundation (Papa et al., 2010a). In addition, hydrological processes in Bangladesh are complicated by the large delta at the confluence of the Ganges and Brahamaputra rivers, which is well captured by satellite (Figs. 4a, c, 6a), but not represented by the model. Conversely, the simulated discharges are clearly overestimated after the monsoon season (October to December). This weakness is not due to the flood scheme because the control experiment exhibits the same behavior. It might be rather linked to the intensive rice irrigation that induces large water pumping from the river or aquifers during this period (Sacks et al. 2009; Roddel et al. 2009; Portmann et al. 2010).

Conversely to Decharme et al. (2008), the experiments with different values of the river bankfull height reveal that the sensitivity of the model is not negligible over many regions of the globe. Note however that the $h_c$ range ($\pm 25\%$) chosen in this study is larger than in Decharme et al. (2008). To sum up, the river bankfull height impacts the land surface evaporation, at least at regional scale, and the range of the increase in evaporation due to the presence of flooded area can be more or less intensive according to the $h_c$ values. An increase in $h_c$ induces a decrease in simulated flooded areas that is not robust compared to the satellite-based estimates and globally deteriorates the simulated river discharge scores compared to *FLD*. The main exception appears over the downstream part of the Mississippi basin where an increase in $h_c$ allows better results. Conversely, a decrease in $h_c$, which induces an increase in simulated flooded areas, is more robust compared to the satellite-based estimates and discharge measurement. Compared to *FLD*, the efficiency scores are improved over 45% of all stations and only reduced over 15%. This improvement in river discharges score is found especially over North America (excluding the downstream part of the Mississippi basin), South America (excluding the Amazon basin), Africa, Australia, and some basins over Eastern Europe (e.g. Volga) and South Asia (Fig. 10b, d). In other words, while $h_c$ could be increased over the Mississippi basin, it also could be decreased over these other regions to improve the model simulations.

This tuning should be based mainly on the river discharge scores, given the large distribution of river gauging measurements over the globe available today, while ensuring a reasonable simulation of the flooded areas compared to the satellite-based estimates. For global hydrological applications such a tuning is certainly not advisable because it should be done with an accurate atmospheric forcing (especially precipitation) which is generally not the case at the global scale. It also could hide some model deficiencies related to the non-representation of irrigation, groundwater dynamics, lakes, large ponds, and wetlands. However for climate studies and from a pragmatic point of view, this tuning could permit to represent the floodplains and especially its related direct evaporation with a reasonable accuracy while the spatio-temporal variations in precipitation are generally poorly represented.

## 6 Conclusions

This study describes the evaluation of the ISBA-TRIP flood model that will be used for global hydrological and climate applications. It is evaluated over the globe using off-line simulations at a 1° by 1° resolution driven by the 1986–2006 3-hourly atmospheric forcing from Princeton University. The flood scheme accounts explicitly for the precipitation interception by the floodplains, the direct evaporation from the free water surface and the possible re-infiltration into the soil. The simulated river discharges are evaluated against 122 in situ gauging measurements distributed all over the globe, while the simulated flooded areas are compared to satellite-derived inundation estimates from Prigent et al. (2007) and an alternative product using jointly the GLWD database of lakes, wetlands and floodplains (Lehner and Döll 2004) and the MIRCA2000 crop irrigation product (Portmann et al. 2010).

The results suggest that the proposed simple flood scheme generally provides a reasonable estimation of the spatio-temporal variability of flooded areas. In addition, the simulated river discharges are improved by this scheme for the majority of the gauging stations affected by floods. This positive impact is mainly related to: (1) an increase in evapo-transpiration and then a decrease in river discharges especially relevant over the regions where the simulated river discharges are overestimated without the flooding scheme; (2) the flood scheme delay and attenuated river peak flow when the floodplain storage is significant. As far as the annual mean water budget is concerned, this increase in evapotranspiration is particularly important at a regional scale and is expected to have a significant regional impact on global climate simulation.

Nevertheless, some deficiencies appear throughout the model evaluation. Different reasons can account for such residual biases: uncertainties in the atmospheric forcing (Chapelon et al. 2002; Fekete et al. 2003; Ngo-Duc et al. 2005; Decharme and Douville 2006b), possible anthropogenic influence on the observed discharges, and deficiencies in the ISBA-TRIP model. Further improvements could be made by adding an explicit representation of irrigation, lakes, marshes, and large ponds. Over high latitudes, the

explicit simulation of the permafrost could potentially improve the present results. In addition, the treatment of groundwater in TRIP could be considerably improved by using a two dimensional approach where the water flux between the groundwater and ISBA or the stream reservoir as well as the water exchange between each neighboring grid-cell could be explicitly calculated (Fan et al. 2007; Miguez-Macho et al. 2007). In addition, satellite-derived inundation estimates could also show some limitation as for example over South Asia, which exhibits very large inundation extents throughout the year.

Besides these reasons, some aspects of the scheme are obviously questionable, such as the empirical computation of the river width, the choice of the river bankfull height, the simple computation of the river slope, the simplified geometry of the river stream and flood reservoirs, or the use of the Manning's formula for computing the mass transfer between them. It must be recognized that the most important parameter is the river width because it mainly controls the good simulation of the river height and the river stream flow velocity (Eqs. 1 and 2). With the river bankfull depth, it controls also the potential mass of water that can be flooded (Eq. 6). The accurate computation of the river slope and/or the value of the Manning's n coefficient are secondary but could help to refine the ISBA-TRIP simulations. The choice of these parameters in this study appear reasonable for this scheme that has been developed for global climate applications, at a relatively low horizontal resolution (0.5° to 1° resolution), and that must be as robust as possible to be applicable over all regions of the world. This first attempt represents another step toward the representation of all inland water bodies in climate simulations. Other limitations are the resolutions of the Digital Elevation Model (DEM) that can induce an underestimation of the simulated flooded fraction through a failure to represent very flat regions or areas smaller than the horizontal and vertical resolution of the DEM (Coe 1998; Coe et al. 2008).

Finally, the sensitivity experiments reveal the non-negligible impact of the river bankfull height on the quality of the simulated flooded areas and river discharges. It also impacts the intensity of the land surface evaporation increase. These results underline that the river bankfull height is potentially tunable region by region. However, such a tuning must be taken with caution on the global scale for at least two reasons:

(1) it might be sensitive to the experimental conditions and especially to the quality of the prescribed atmospheric forcing which is less robust than at a regional scale;
(2) it could mask the model deficiencies related to the non-representation of irrigation, groundwater dynamics, lakes, large ponds, and wetlands.

Another way could be suggested: the development of a global database describing the major river characteristics as the stream width and the river bankfull height. Such a database would be an important progress for future hydrological developments.

**Acknowledgments** This work is supported by the program IMPACT-BOREAL of the French "Agence Nationale pour la Recherche" (ANR), the CYMENT project of the RTRA STAE Toulouse, the "Centre National de Recherches Météorologiques" (CNRM) of Météo-France, and the "Centre National de la Recherche Scientifique" (CNRS) of the French research ministry. The authors would like to thank Christine Delire (CNRS/CNRM) as well as anonymous reviewers for their useful comments on this study.

## Appendix

### The floodplain dynamics

The flood inflow and outflow velocities computed using the Manning's formula (Eq. 7) requires the hydrological slope between the floodplain and the river stream:

$$\begin{cases} s_{in} = \dfrac{\max\left(0, h_s - h_c - h_f\right)}{\left(W + W_f\right)/2} \\ s_{out} = \dfrac{\max\left(0, h_f + h_c - h_s\right)}{\left(W + W_f\right)/2} \end{cases} \quad \text{(A1)}$$

They also require the hydraulic radius assumed rectangular and calculated as follows:

$$\begin{cases} R_{in} = \dfrac{L_f \times \max(0, h_s - h_c)}{L_f + 2 \times \max(0, h_s - h_c)} \\ R_{out} = \dfrac{L_f h_f}{L_f + 2h_f} \end{cases} \quad \text{(A2)}$$

where $W_f$ (m), $L_f$ (m) and $h_f$ (m) are the width, the length and the depth of the floodplains, $h_s$ (m) the water height of the stream reservoir, $h_c$ (m) the critical height of the river bed, and $W$ (m) the stream river width.

$h_f$ is calculated in each grid-cell with the help of the actual distribution of the local height, $h_i$ (m), determined at a 1 km by 1 km resolution. The assumption is that each pixel, $i$, represents a sub-basin into a given grid-cell that can be potentially flooded as shown in Fig. 14a. Each sub-basin has a triangular form and is associated with a fraction, $f_i$, of the grid cell area, $A$. $h_i$ is computed using the local slope, $\sigma_i$ (°), and flow direction data given by the HYDRO1 K data set (Verdin and Greenlee 1996) at 1 km resolution:

$$h_i = l\sqrt{\alpha_i}\tan\left(\sigma_i \frac{\pi}{180}\right) \quad \text{(A3)}$$

where $l$ (m) is the characteristic length of one pixel equal to 1,000 m, and $\alpha_i$ is equal to 1 if the local flow direction is

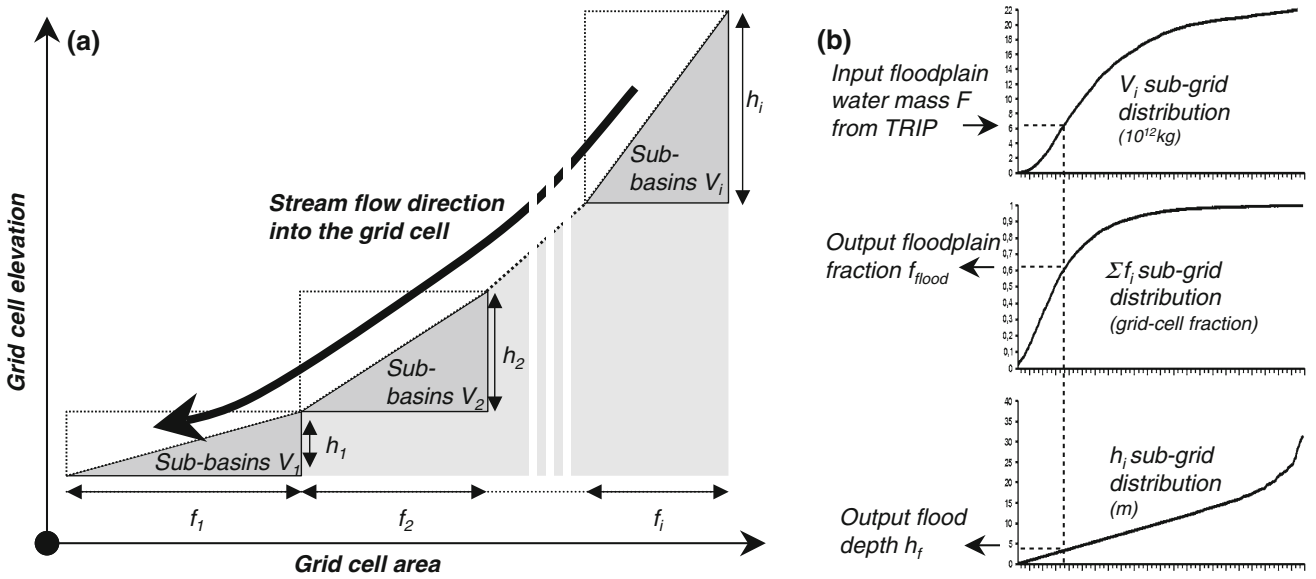


**Fig. 14** Schematic representation of the floodplain sub-grid scheme. **a** One grid-cell is approximated as an individual basin where the water flows from the largest to the flattest slope of each pixel at 1 km resolution. Each pixel is then assumed as a sub-basin that can be potentially flooded. These pixels are ranked from the lower to the higher depth, $h_i$, computed according to the slope of each pixel. Then, a sub-grid area, $f_i$, and a potential water mass, $V_i$, can be associated with each entity. **b** The comparison of the floodplain water mass, $F$, computed by TRIP with the $V_i$ sub-grid distribution permits to find the associated floodplain fraction, $f_{flood}$, and flood depth, $h_f$, into the grid cell via the sub-grid distribution of $f_i$ and $h_i$, respectively

north, south, east, or west, and to 2 elsewhere. Therefore, for each $h_i$ a potential mass of flood, $V(h_i)$ (kg), can be simply calculated using a discrete equation:

$$V(h_i) = \rho_w \sum_0^i V_i \quad \text{where} \quad V_i = \frac{A f_i h_i}{2} \tag{A4}$$

As shown in Fig. 14b, the sub-grid distributions of the flooded fraction and the flood depth allow to determine $f_{flood}$, and $h_f$ at each time step and in each grid-cell via the comparison between the water mass into the floodplain reservoir, $F$, computed by TRIP (Eq. 4) and the sub-grid distribution of this potential mass $V(h_i)$:

$$F = V(h_i) \Rightarrow \left| \begin{array}{l} f_{flood} = \sum_0^i f_i \\ h_f = h_i \end{array} \right. \tag{A5}$$

When $f_{flood}$ is known within the grid cell, $W_f$ and $L_f$ are simply calculated as follow:

$$\left| \begin{array}{l} L_f = \max\left(0.001, r\sqrt{f_{flood} A}\right) \\ W_f = \dfrac{A f_{flood}}{L_f} \end{array} \right. \tag{A6}$$

where $r$ is the meandering ratio fixed to 1.4 as recommended by Oki and Sud (1998).

Finally, because ISBA uses a single surface temperature, a new fraction, $p_{ff}$, is added in each grid cell to account for the effect of the floodplains on the surface energy budget. A fraction of vegetation masked by the floodplains, $p_{f,veg}$, is estimated and combined with the TRIP flooded fraction, $f_{flood}$, as follows to limits the floodplain evaporation under dense canopy:

$$\left| \begin{array}{l} p_{f,veg} = f_{flood} \times \min\left[1, \dfrac{3}{LAI}\right] \\ p_{ff} = (1 - veg) f_{flood} + veg\, p_{f,veg} \end{array} \right. \tag{A7}$$

where $LAI$ (m.m$^{-1}$) is the leaf area index given by the ECOCLIMAP data base and $veg$ the dimensionless fraction of the vegetation in each grid cell. According to the ECOCLIMAP database, the LAI is generally inferior to 3 for low vegetation (e.g., grassland, crops) and superior for high vegetation (e.g., trees, forests). Then, the direct evaporation (or sublimation if the surface temperature is inferior to 0°C), $E_f$ (Kg.m$^{-2}$), from this flooded fraction is simply estimated by:

$$E_f = p_{ff} \rho_a C_H V_a [q_{sat}(T_s) - q_a] \tag{A8}$$

where $\rho_a$ (kg.m$^{-3}$) is the air density, $q_a$ (kg.kg$^{-1}$) the air humidity, $V_a$ the wind speed (m.s$^{-1}$), $C_H$ the dimensionless drag coefficient depending upon the thermal stability of the atmosphere and $q_{sat}$ (kg.kg$^{-1}$) the saturated specific humidity at the surface that depends on surface temperature, $T_s$ (K).

## References


Alkama MR, Kageyama M, Ramstein G, Marti O, Ribstein P, Swingedouw D (2008) Impact of a realistic river routing in coupled ocean-atmosphere simulations of the Last Glacial Maximum climate. Clim Dyn 30:855–869

Alkama R, Decharme B, Douville E, Becker M, Cazenave A, Sheffield J, Voldoire A, Titeca S, Lemoigne P (2010) Global evaluation of the ISBA-TRIP continental hydrological system. Part 1: A twofold constraint using GRACE terrestrial water storage estimates and in situ river discharges. J Hydrometeor 11:583–600

Alsdorf DE, Rodrıguez E, Lettenmaier DP (2007) Measuring surface water from space. Rev Geophys 45: RG2002. doi:10.1029/2006RG000197

Arora VK, Boer GJ (1999) A variable velocity flow routing algorithm for GCMs. J Geophys Res 104:30965–30979

Arora VK, Chiew FHS, Grayson RB (1999) A river flow routing scheme for general circulation models. J Geophys Res 104:14347–14357

Barnes HH Jr (1967) Roughness characteristics of natural channels. US Geological survey water-supply paper 1849, p. 213

Beighley RE, Eggert KG, Dunne T, He Y, Gummadi V, Verdin KL (2009) Simulating hydrologic and hydraulic processes throughout the Amazon river basin. Hydrol Process 23:1221–1235. doi:10.1002/hyp.7252

Beven KJ, Kirkby MJ (1979) A physically-based variable contributing area model of basin hydrology. Hydrol Sci Bull 24:43–69

Boone A, Masson V, Meyers T, Noilhan J (2000) The influence of the inclusion of soil freezing on simulation by a soil-atmosphere-transfer scheme. J Appl Meteorol 9:1544–1569

Bousquet P, Ciais P, Miller JB, Dlugokencky EJ, Hauglustaine DA, Prigent C, Van der Werf GR, Peylin P, Brunke EG, Carouge C, Langenfelds RL, Lathière J, Papa F, Ramonet M, Schmidt M, Steele LP, Tyler SC, White J (2006) Contribution of anthropogenic and natural sources to atmospheric methane variability. Nature 443:439–443. doi:10.1038/nature05132

Chapelon N, Douville H, Kosuth P, Oki T (2002) Off-line simulation of the Amazon water balance: a sensitivity study with implications for GSWP. Climate Dyn 19:141–154

Coe M (1998) A linked global model of terrestrial processes: simulation of modern rivers, lakes and wetlands. J Geophys Res 103:8885–8899

Coe MT, Costa MH, Botta A, Birkett C (2002) Long-term simulation of discharge and floods in the Amazon basin. J Geophys Res 107(D20): 8044. doi:10.1029/2001JD000740

Coe MT, Costa MH, Howard EA (2008) Simulating the surface waters of the Amazon River basin: impact of new river geomorphic and flow parameterizations. Hydrol Proc 22:2542–2553. doi:10.1002/hyp.6850

Cogley JG (2003) GGHYDRO—global hydrographic data, release 2.3. Trent Tech Note 2003-1, Department of Geography, Trent University, Peterborough, Canada, 11 pp. Available online at http://people.trentu.ca/∼gcogley/glaciology/index.htm

Dadson SJ, Ashpole I, Harris P, Davies HN, Clark DB, Blyth E, Taylor CM (2010) Wetland inundation dynamics in a model of land surface climate: evaluation in the Niger inland delta region. J Geophys Res 115:D23114. doi:10.1029/2010JD014474

Decharme B, Douville H (2006a) Introduction of a sub-grid hydrology in the ISBA land surface model. Clim Dyn 26:65–78

Decharme B, Douville H (2006b) Uncertainties in the GSWP-2 precipitation forcing and their impacts on regional and global hydrological simulations. Clim Dyn 27:695–713

Decharme B, Douville H (2007) Global validation of the ISBA sub-grid hydrology. Clim Dyn 29:21–37. doi:10.1007/s00382-006-0216-7

Decharme B, Douville H, Boone A, Habets F, Noilhan J (2006) Impact of an exponential profile of saturated hydraulic conductivity within the ISBA LSM: simulations over the Rhône Basin. J Hydrometeor 7:61–80

Decharme B, Douville H, Prigent C, Papa F, Aires F (2008) A niew river flooding scheme for global climate applications: off-line evaluation over South America. J Geophys Res 113:D11110. doi:10.1029/2007JD009376

Decharme B, Alkama R, Douville E, Becker M, Cazenave A (2010) Global evaluation of the ISBA-TRIP continental hydrologic system. Part 2: Uncertainties in river routing simulation related to flow velocity and groundwater storage. J Hydrometeor 11:601–617

Dirmeyer PA (2000) Using a global soil wetness data set to improve seasonal climate simulation. J Clim 13:2900–2922

Dirmeyer PA (2001) Climate drift in a coupled land–atmosphere model. J Hydrometeor 2:89–100

Douville H (2003) Assessing the influence of soil moisture on seasonal climate variability with AGCMs. J Hydrometeor 4:1044–1066

Douville H (2004) Relevance of soil moisture for seasonal atmospheric predictions: is it an initial value problem? Clim Dyn 22:429–446

Douville H, Viterbo P, Mahfouf JF, Beljaars ACM (2000a) Validation of the optimum interpolation technique for sequential for soil moisture analysis using Fife data. Mon Wea Rev 128:1733–1756

Douville H, Planton S, Royer JF, Stephenson DB, Tyteca S, Kergoat L, Lafont S, Betts RA (2000b) Importance of vegetation feedbacks in doubled-CO2 climate experiments. J Geophys Res 105(D11):14841–14861

Ducharne A, Golaz C, Leblois E, Laval K, Polcher J, Ledoux E, de Marsily G (2003) Development of a high resolution runoff routing model: calibration and application to assess runoff from the LMD GCM. J Hydrol 280:207–228

Durand F, Papa F, Rahman A, Bala SK (2010) Impact of Ganges-Brahmaputra interannual discharge variations on Bay of Bengal salinity and temperature during the 1992–99 period. J Earth Syst Sci (revised)

Fan Y, Miguez-Macho G (2010) A simple hydrologic framework for simulating wetland in climate and earth system models. Clim Dyn. doi:10.1007/s00382-010-0829-8 (On-line First)

Fan Y, Miguez-Macho G, Weaver C-P, Walko R, Robock A (2007) Incorporing water table dynamics in climate modeling: 1. Water table observations and equilibrium water table simulations. J Geophys Res 112:D10125. doi:10.1029/2006JD008111

FAO/IIASA/ISRIC/ISSCAS/JRC (2009) Harmonized World Soil Database (Version 1.1). FAO, Rome, Italy and IIASA, Laxenburg, Austria (http://www.iiasa.ac.at/research/LUC/External-World-Soil6database/HTML/)

Fekete BM, Vörösmarty CJ, Road JO, Willmott CJ (2003) Uncertainties in precipitation and their impacts on runoff estimates. J Clim 17:294–304

Frappart F, Papa F, Güntner A, Werth S, Ramillien G, Prigent C, Rossow WB, Bonnet M-P (2010) Interannual variations of the terrestrial water storage in the Lower Ob' basin from a multisatellite approach. Hydrol Earth Syst Sci 14:2443–2453. doi:10.5194/hess-14-2443-2010

Gedney N, Cox PM, Douville H, Polcher J, Valdes PJ (2000) Characterizing GCM land surface schemes to understand their responses to climate change. J Clim 13:3066–3079

Gedney N, Cox PM, Huntingford C (2004) Climate feedback from wetland methane emission. Geophys Res Lett 31:L20503. doi:10.1029/2004GL020919

Güntner A, Stuck J, Werth S, Döll P, Verzano K, Merz B (2007) A Global analysis of temporal and spatial variations in continental water storage. Water Resour Res 43:W05416. doi:10.1029/2006WR005247

Hagemann S, Dümenil L (1998) A parameterization of lateral water flow for the global scale. Clim Dyn 14:17–41
Hansen MC, Defries RS, Townshend JRG, Sohlberg R (2000) Global land cover classification at 1 km spatial resolution using a classification tree approach. Int J Remote Sens 21:1331–1364
Houweling S, Kaminski T, Dentener F, Lelieveld J, Heinmann M (1999) Inverse modeling of methane sources and sinks using adjoint of a global transport model. J Geophys Res 104:26137–26160
Knighton E (1998) Fluvial forms and processes: a new perspective. Edward Arnold, London
Koster RD, Suarez M, Ducharne A, Stieglitz M, Kumar P (2000) A catchment-based approach to modeling land surface processes in a GCM—Part 1: model structure. J Geophys Res 105(D20):24809–24822
Koster RD, Dirmeyer PA, Hahmann AN, Ijpelaar R, Tyahla L, Cox P, Suarez MJ (2002) Comparing the degree of land–atmosphere interaction in four atmospheric general circulation models. J Hydrometeor 3:363–375
Kouraev A, Zakharova EA, Samain O, Mognard-Campbell N, Cazenave A (2004) Ob river discharge from Topex/Poseidon satellite altimetry. Remote Sens Environ 93:238–245
Krinner G (2003) Impact of lakes and wetlands on boreal climate. J Geophys Res 108(D16): 4520. doi:10.1029/2002JD002597
Lawrence DM, Slater AG (2007) Incorporating organic soil into a global climate model. Clim Dyn 30(2–3):145–160
Leduc C, Bromley J, Schroeter P (1997) Water table fluctuation and recharge in semi-arid climate: some results of the HAPEX-Sahel hydrodynamic survey (Niger). J Hydrol 188–189:123–138
Leduc C, Favreau G, Schroeter P (2001) Long term rise in a Sahelian water-table: the continental terminal in South-West Niger. J Hydrol 243:43–54
Lehner B, Döll P (2004) Developement and validation of a global database of lakes, reservoirs and wetlands. J Hydrol 296:1–22
Liston GE, Sud C, Wood EF (1994) Evaluating GCM land surface hydrology parameterizations by computing river discharges using a runoff routing model: application to the Mississipi basin. J Appl Meteor 33: 394–405
Lucas-Picher P, Arora VK, Caya D, Laprise R (2003) Implementation of a large-scale variable velocity flow routing algorithm in the Canadian Regional Climate Model (CRCM). Atmosphere-Ocean 41:139–153
Manning R (1891) On the flow of water in open channels and pipes. Inst Civil Eng Ireland Trans 20:161–207
Masson V, Champeaux J-L, Chauvin C, Meriguet C, Lacaze R (2003) A global database of land surface parameters at 1 km resolution for use in meteorological and climate models. J Clim 16:1261–1282
Matthews E (2000) Wetlands, in Atmospheric methane: its role in the global environment. In Khalil MAK (ed). Springer, New York. pp 202–233
Miguez-Macho G, Fan Y, Weaver C-P, Walko R, Robock A (2007) Incorporating water table dynamics in climate modeling: 2. Formulation, validation, and soil moisture simulation. J Geophys Res 112:D13108. doi:10.1029/2006JD008112
Miller JR, Russel GL, Caliri G (1994) Continental-scale river flow in climate models. J Clim 7: 914–928
Molod A, Salmun H, Waugh D (2004) The impact on a GCM climate of an extended mosaic technique for the land-atmosphere coupling. J Clim 17:3877–3891
Moody JA, Troutman BM (2002) Characterization of the spatial variability of channel morphology. Earth Surf Process Landforms 27:1251–1266
Nash JE, Sutcliffe V (1970) River forecasting through conceptual models. J Hydrol 10:282–290
Ngo-Duc T, Polcher J, Laval K (2005) A 53-year forcing data set for land surface models. J Geophys Res 110:D06116. doi:10.1029/2004JD005434
Ngo-Duc T, Oki T, Kanae S (2007) A variable streamflow velocity method for global river routing model: model description and preliminary results. Hydrol Earth Syst Sci Discuss 4:4389–4414
Noilhan J, Planton S (1989) A simple parameterization of land surface processes for meteorological models. Mon Wea Rev 117:536–549
Oki T, Sud YC (1998) Design of total runoff integrating pathways (TRIP). A global river channel network. Earth Inter 2:1–36
Papa F, Prigent C, Rossow WB (2007) Ob' River flood inundations from satellite observations: a relationship with winter snow parameters and river runoff. J Geophys Res 112:D18103. doi:10.1029/2007JD008451
Papa F, Prigent C, Rossow WB (2008) Monitoring flood and discharge variations in the large Siberian rivers from a multi-satellite technique. Surv Geophys 29:297–317. doi:10.1007/s10712-008-9036-0
Papa F, Prigent C, Aires F, Jimenez C, Rossow WB, Matthews E (2010a) Interannual variability of surface water extent at the global scale, 1993–2004. J Geophys Res 115:D12111. doi:10.1029/2009JD012674
Papa F, Durand F, Rossow WB, Rahman A, Bala S (2010b) Satellite altimeter-derived monthly discharge of the Ganga-Brahmaputra River and its seasonal to interannual variations from 1993 to 2008. J Geophys Res 115:C12013. doi:10.1029/2009JC006075
Portmann FT, Siebert S, Döll P (2010) Global monthly irrigated and rainfed crop areas around the year 2000: a new hight-resolution data set for agricultural and hydrological modeling. Global Biogeochem Cycles 24: GB1011. doi:10.1029/2008GB003435
Price JS, Branfireum BA, Waddington JM, Devito KJ (2005) Advances in Canadian wetland hydrology, 1999–2003. Hydrol Process 19:201–214
Prigent C, Matthews E, Aires F, Rossow WB (2001) Remote sensing of global wetland dynamics with multiple satellite data set. Geophys Res Lett 28:4631–4634
Prigent C, Papa F, Aires F, Rossow WB, Matthews E (2007) Global inundation dynamics inferred from multiple satellite observations, 1993–2000. J Geophys Res 112:D12107. doi:10.1029/2006JD007847
Ringeval B, de Noblet-Ducoudré N, Ciais P, Bousquet P, Prigent C, Papa F, Rossow WB (2010) An attempt to quantify the impact of changes in wetland extent on methane emissions on the seasonal and interannual time scales. Global Biochem Cycles 24: GB2003. doi:10.1029/2008GB003354
Roddel M, Velicogna I, Famiglietti JS (2009) Satellite-based estimates of groundwater depletion in India. Nature 460:999–1003. doi:10.1038/nature08238
Sacks WJ, Cook BI, Buenning N, Levis S, Helkowski JH (2009) Effects of global irrigation on the near-surface climate. Clim Dyn 33. doi:10.1007/s00382-008-0445-z
Sheffield J, Goteti G, Wood EF (2006) Development of a 50-year high-resolution global data set of meteorological forcings for land surface modeling. J Clim 19:3088–3111
Shindell DT, Falugevi G, Bell N, Schmidt GA (2004) An emission-based view of climate forcing by methane and tropospheric ozone. Geophys Res Lett 32. doi:10.1029/2004GL021900
Thomas H, Nisbet TR (2006) An assessment of the impact of floodplains woodland on flood flow. Water Environ J 21:114–126
Verdin KL, Greenlee SK (1996) Development of continental scale digital elevation models and extraction of hydrographic features. In Proceedings, third international conference/workshop on integrating GIS and environmental modeling, Santa Fe, New Mexico, January 21–26, 1996. National Center for Geographic Information and Analysis, Santa Barbara
Vörösmarty CJ, Moore B, Grace AL, Gildea MP, Melillo JM, Peterson BJ, Rastetter EB, Steudler PA (1989) Continental scale models of water balance and fluvial transport : an application to South America. Global Biogeochem Cycles 3: 241–265